TÜRKİYE CUMHURİYETİ
ADANA ALPARSLAN TÜRKEŞ SCIENCE AND TECHNOLOGY UNIVERSITY

GRADUATE SCHOOL
ELECTRICAL AND ELECTRONIC ENGINEERING DEPARTMENT

REMOVAL OF HAIR ARTIFACTS IN SKIN LESION IMAGES AND ITS IMPACT ON SKIN CANCER DETECTION

BERCESTE YILMAZ

M.Sc.

ADANA 2024

TÜRKİYE CUMHURİYETİ
ADANA ALPARSLAN TÜRKEŞ SCIENCE AND TECHNOLOGY UNIVERSITY

GRADUATE SCHOOL
ELECTRICAL AND ELECTRONIC ENGINEERING DEPARTMENT

REMOVAL OF HAIR ARTIFACTS IN SKIN LESION IMAGES AND ITS IMPACT ON SKIN CANCER DETECTION

BERCESTE YILMAZ

M.Sc.

THESIS ADVISOR
ASST.PROF. DR. AMİRA TANDİROVİÇ GÜRSEL

ADANA, 2024

ÖZET

CİLT LEZYON GÖRÜNTÜLERDE SAÇ ARTEFAKTLARININ ÇIKARILMASI VE CİLT KANSERİ TEŞHİS DOĞRULUĞUNA ETKİSİ

Berceste YILMAZ

Yüksek Lisans, Elektrik-ElektronikAnabilim Dalı

Danışman: Dr.Öğr.Üye. Amira TANDİROVİÇ GÜRSEL

Kasım 2024, 81 sayfa

Kanserin erken tanısı, tedavi ve prognoz başarısında önemli faktörlerden biridir. Son yıllarda, cilt kanseri insidansı dünya genelinde artış göstermiştir ve bu durum, erken teşhisin hasta sonuçlarını iyileştirme açısından kritik hale gelmesine neden olmuştur. Bu çalışma, cilt lezyonu verilerinin bütünlüğünü bozmadan dermatoskopik görüntülerden kıl eserlerini ortadan kaldıran gelişmiş kıl giderme filtreleri geliştirerek cilt kanseri teşhisini iyileştirmeye odaklanmıştır. Geleneksel yöntemler, örneğin Dullrazor filtresi, özellikle yoğun saç örtüsüne sahip görüntülerde hem açık hem de koyu saçları etkili bir şekilde çıkarma konusunda sınırlamalar göstermiştir. Buna karşılık, bu araştırma, Wiener filtreleme, blackhat dönüşümü ve adaptif eşikleme gibi teknikleri birleştirerek ve ardından saçın çıkarıldığı alanları geri yüklemek için görüntü doldurma işlemi ile yeni saç çıkarma algoritmaları sunmaktadır. Bu yöntemler, HAM10000 veri seti üzerinde test edilmiş ve deri lezyonu teşhis doğruluğu üzerindeki etkileri açısından mevcut yaklaşımlarla karşılaştırılmıştır.

Sonuçlar, geliştirilen yeni filtrelerin, saç artefaktlarını etkili bir şekilde ortadan kaldırırken lezyon özelliklerini koruyarak melanoma tespit doğruluğunu önemli ölçüde artırdığını göstermektedir. Ayrıca, bu çalışmada geliştirilen geliştirilmiş ön işleme tekniklerinin, erken evre teşhis için daha güvenilir ve verimli bir çözüm sunarak, cilt kanseri tespiti için derinöğrenme modellerine entegre edilme potansiyeli vurgulanmıştır. Bulgular, tıbbi görüntü analizi bağlamında sağlam bir görüntü ön işlemeyi vurgulayarak CAD sistemlerinin iyileştirilmesine yönelik devam eden çabalara katkıda bulunacaktır.

Anahtar Kelimeler: Cilt kanseri tespiti, Saç çıkarma, Dermoskopik görüntüler, Derin Öğrenme, Xception algoritması.

ABSTRACT

REMOVAL OF HAIR ARTIFACTS IN SKIN LESON IMAGES AND ITS IMPACT ON SKIN CANCER DETECTION ACCURACY

Berceste YILMAZ

M.Sc., Department of Electrical and Electronic Engineering

Supervisor: Assoc. Prof. Dr. Amira TANDİROVİÇ GÜRSEL

November 2024, 81 pages

Early cancer diagnosis is one of the important factors in successful treatment and prognosis. In recent years, the incidence of skin cancer has risen globally, making early diagnosis critical for improving patient outcomes. This study focuses on improving skin cancer diagnosis by developing advanced hair removal filters that eliminate hair artefacts from dermoscopic images without compromising the integrity of skin lesion data. Traditional methods, such as the Dullrazor filter, have shown limitations in effectively removing both light and dark hairs, especially in images with dense hair coverage. In response, this research introduces novel hair removal algorithms that combine techniques like Wiener filtering, blackhat transformation, and adaptive thresholding, followed by image inpainting to restore the hair-removed areas. These methods have been tested on the HAM10000 dataset and compared with existing approaches in terms of their impact on skin lesion diagnosis accuracy.

The results demonstrate that the newly developed filters significantly improve the accuracy of melanoma detection by preserving essential lesion features while effectively removing hair artefacts. Furthermore, the study highlights the potential of these enhanced pre-processing techniques to be integrated into deep learning models for skin cancer detection, offering a more reliable and efficient solution for early-stage diagnosis. The findings will contribute to the ongoing efforts to refine CAD systems emphasizing the importance of robust image pre-processing in the context of medical image analysis.

Keywords: Skin cancer detection, Hair removal, Dermoscopic images, Deep Learning, Xception algorithm

Dedication

to my wonderful deeply missed mom…

ACKNOWLEDGEMENTS

First and foremost, I would like to extend my heartfelt gratitude to my supervisor. She has been far more than a mentor to me; her unwavering support and belief in my potential encouraged me to strive for excellence. Words cannot fully convey my appreciation for her guidance and inspiration along this journey.

I am deeply grateful to my esteemed colleagues, especially my colleague Res. Asst. Barış Aydın, for the unwavering belief in my success and the support they have given me.

Lastly, I am profoundly thankful to my family. In moments when I felt overwhelmed or uncertain, they lifted my spirits and helped me find hope for a brighter tomorrow. Their encouragement made this endeavor possible.

TABLE OF CONTENTS

LIST OF FIGURES

LIST OF TABLES

LIST OF ABBREVIATIONS

WHO	: The World Health Organization
NMSC	: Non-melanoma Skin Cancer
CAD	: Computer-based skin cancer diagnosis system
ML	: Machine learning
DL	: Deep learning
UV	: Ultraviolet
BCC	: Basal cell carcinoma
SCC	: Squamous cell carcinoma
AK	: Actinic keratosis
AI	: Artificial intelligence
ANN	: Artificial neural network
DNN	: Deep neural network
CNN	: Convolutional neural network
ILSVRC	: ImageNet Large Scale Visual Recognition Challenge
VGG	: The Visual Geometry Group
ILSVRC14	: 2014 ImageNet Large-Scale Visual Recognition Challenge
ResNet	: Residual Network
DenseNet	: Densely Connected Network
ISIC	: International Skin Imaging Collaboration
ROI	: Region of interest
ESRGAN	: Enhanced Super Resolution Generative Adversarial Networks
SNR	: Signal-to-noise ratio
LDA	: Linear discriminant analysis
CLAHE	: Contrast-limited adaptive histogram equalization
FMM	: Fast Marching Method
LoG	: Laplacian of Gaussian
RGB	: Red, green, blue
GUI	: Graphical user interface

LIST OF SYMBOLS

$\boldsymbol{w_0}$	**:** Bias
$\boldsymbol{g}$	**:** Activation function
$\boldsymbol{w_i}$	**:** Input weight
$\boldsymbol{t}$	**:** Time
$\boldsymbol{h(k)}$	**:** Impulse response
$\boldsymbol{C}$	**:** Constant
$\boldsymbol{exp}$	**:** Exponential
∇^2	**:** Laplacian operator

1. INTRODUCTION

Cancer is a group of diseases caused by the uncontrolled proliferation of abnormal cells in any region of the human body, often followed by spreading to other organs threatening people's health and life. In a healthy body, during the life cycle, any cell grows, divides and dies. In that fully controlled process, damaged or old cells are replaced by newly formed ones. However, sometimes some of the cells do not follow this process and perform uncontrollable growth, and instead of dying, they pursue producing new abnormal cells. These abnormal cells may constitute solid or liquid tumors, which can be cancerous or benign [1, 2]. Benign tumors do not tend to spread to other parts of the body and remain in their original position. They usually develop gradually and also have clear boundaries. These are generally not an issue unless they become huge and pressure adjacent structures, resulting in pain or other health problems. However, for several reasons, some of them may transform into cancerous tumors over time. Unlike benign ones, cancerous tumors tend to diffuse in neighboring tissues and migrate to further areas of the human body, using either blood vessels or the lymphoid system, to generate new tumors. It is called metastasis, which can develop in any part of the body [2, 3]. Approximately 90% of cancer deaths are attributed to metastasis, with limited progress made in its treatment [4].

The World Health Organization (WHO) states that cancer is a major cause of mortality, responsible for nearly 10 million deaths each year, globally. Although lung, breast, and colon are the most frequent cancer types worldwide, skin cancer is one of the most diagnosed cancers in developed countries [5]. Table 1.1 provides a detailed breakdown of WHO Global Cancer statistics by mortality numbers and population [6]. Multiple different forms of cancer can emerge in various organs and body tissues. Depending on the peculiarities of the location where it first forms, each type of cancer has unique symptoms and spread patterns. For example, lung cancer arises in the respiratory pathways, breast cancer in the tissue of the breast, and skin cancer in the external skin layers. It should be highlighted that prevalence is important but not the sole parameter affecting mortality. Other parameters that should be considered are invasiveness and sub-type. That is, some less frequent but more invasive varieties, such as brain and pancreatic cancers, could be more fatal than their more frequent counterparts. On the same

lines, each subtype has a characteristic disease pattern, rate of spread, and response to treatment, so the treatment techniques. Early detection procedures also vary from type to type.

Skin cancer develops on the cells of the skin tissue and can be classified into two primary categories: nonmelanoma and melanoma. Non-melanoma skin cancer (NMSC) is a rather large group with not only one of the highest prevalence but also a small mortality among cancers globally [7, 8]. Due to its commonality and ease of treatment, it has not been adequately included in cancer registries in many countries [8-10]. On the other hand, melanoma is believed to be one of the most fatal of all cancers. On the other hand, melanoma is believed to be one of the deadliest of all cancers. Although melanoma is not included in the top 3, it is important to highlight that its prevalence is visibly increasing.[11].

Table 1.1. WHO Global Cancer Statistics by Mortality Numbers and Population, 2020

POPULATION	THE NUMBER OF MORTALITY
Africa	754,574
Latin America and the Caribbean	741,152
Northern America	700,726
Europe	1,972,982
Oceania	72,558
Asia	5,432,424
Total	9,674,416

Early diagnosis of skin cancer is crucial for efficient treatment. Skin cancer diagnosis generally initiates with self-examinations and culminates with clinical evaluations by a dermatologist. Some symptoms to look out for are new or changing skin spots, moles, and lesions that change color, size, or shape [12]. Skin cancer can only be diagnosed by a dermatologist. Dermatologists may closely inspect suspected lesions using a dermatoscope, also known as a skin microscope, which helps to evaluate skin lesions and diagnose skin cancer. It employs lenses and a lighting source to magnify the lesion structures that are not visible to the naked eye. However, these instruments are rather expensive and not widely available, and their use requires comprehensive training, as well. These obstacles lead to novel pursuits in skin cancer diagnosis, one of which is a computer-based skin cancer diagnosis system (CADs).

CADs have been developed to diagnose skin cancer in its early stage from images of lesions benefiting from one of several machine learning (ML) and deep learning (DL) algorithms. The

algorithm is selected considering several parameters such as the size and type of dataset, computational resources, and time response. Within experimental circumstances, studies demonstrated that computerized analysis systems have the ability to diagnose melanoma [13]. CADs generally consist of five steps: image acquisition, preprocessing, segmentation, feature extraction and classification. DL-based approaches outperformed other computer-based methods in either segmentation or categorization of skin lesions due to their capacity to extract complex characteristics from skin lesion photos in greater detail. They are substantially more efficient than other approaches in learning task-specific properties [14,15].

This study aims to improve preprocessing by developing various hair removal filters to get rid of hair with minimal damage to skin lesions. The outputs of 5 filters and the original images are used in the constitution of a new dataset processed by Xception algorithm to classify the images into two categories malignant and benign.

2. THEORETICAL BACKGROUND

2.1. Skin Cancer

2.1.1. Skin

Skin, whose structure is shown in Figure 2.1, is the largest organ of the human body, with a surface area of 1.5–2 m^2 in an average adult and accounts for 7% of total body weight [16]. Skin acts as a barrier, separating the outside world from the body and keeping hazardous materials from accessing the interior of the body. It also preserves the temperature of the body. In some regions, the skin includes structures such as nails, hair, and blood vessels. Skin consists of tissue layers, termed the epidermis, dermis, and hypodermis (subcutaneous tissue). Each of them is composed of various tissues and has specific functions.

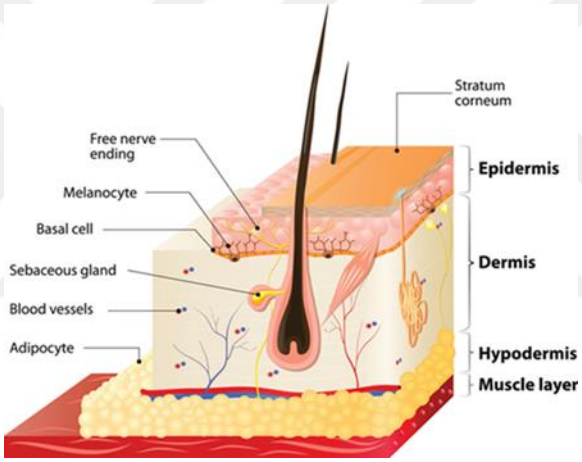

Figure 2.1. The diagram shows the structure of skin. Skin has three layers which are called epidermis, dermis, and hypodermis (subcutaneous tissue) [17]

The epidermis is the outermost layer of the skin. It is composed of layers called strata. The thickness of the epidermis varies at different sites of the body. The cells known as keratinocytes are predominantly found in the epidermis and contribute to the skin's protective characteristics. Following an injury, these cells produce antimicrobial peptides that help shield the skin from pathogens like bacteria. They also synthesize keratin, a fibrous protein. Melanocytes are cells located in the lowest layers of the epidermis that produce a pigment called melanin. The pigment shields the skin from the damaging impacts of ultraviolet (UV) radiation in the sun. The synthesis of melanin, which influences skin color, is determined by an individual's heredity. Melanocytes generate more melanin in people with darker skin than in those with lighter skin.

Sunlight activates melanocytes, increasing melanin synthesis to protect the skin from UV radiation. However, excessive sun exposure can lead to skin cancer by altering the DNA structure of the melanin protein [18-20].

The dermis, which is found underneath the epidermis, has an elastic and robust structure. It contains plenty of fibroblasts, macrophages, and mast cells. Fibroblast cells create collagen and elastin fibers, which provide the dermis elasticity. The dermis supplies nourishment to the epidermis via blood vessels. Unlike the epidermis, it also includes nerves, sensory receptors, hair follicles, sebaceous glands, and sweat glands [18-20].

The hypodermis, the deepest layer of skin, has several functions. It links the dermis layer of the skin to muscles and bones. Besides, it prevents the skin from rubbing against the underlying tissues and muscles, enabling it to move easily on them. This layer contains structures such as blood vessels, hair follicles, nerves, sweat glands, and macrophages [21].

Cancer is a disease that causes cells in any region of the human body to proliferate uncontrolled and spread from one location to another. It is called from the area in the organs where it begins. Skin cancer, as the name implies, refers to potentially lethal lesions on the skin. It arises as a result of uncontrolled growth of abnormal cells in the top layer of the skin caused by alteration of normal skin cells' cycle of activities resulting in a huge abundance of cancer cells.

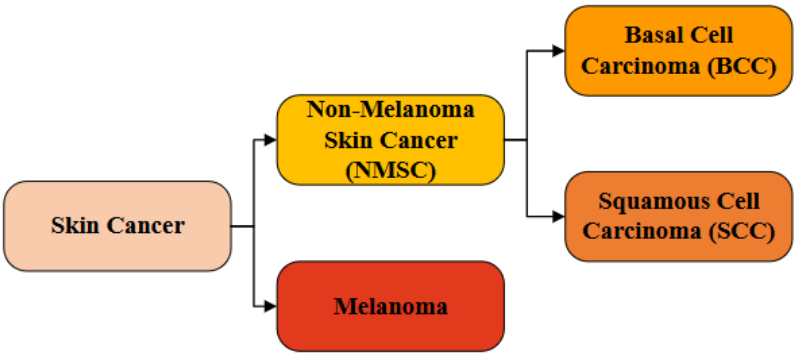

Figure 2.2. The diagram of skin cancer classification

Skin cancer is classified into two major types: non-melanoma skin cancer and melanoma. Non-melanoma skin cancer consists of basal cell carcinoma and squamous cell carcinoma. The diagram of skin cancer is shown in Figure 2.2. Basal cell carcinoma is the most common and appears as a glossy, pearly lump on sun-exposed skin [22]. Squamous cell carcinoma, which

develops in the outer skin layer, typically appears as a hard, red nodule or a flat lesion with a scaly surface [23]. Melanoma, the most aggressive kind, develops in melanocytes, which are responsible for pigment synthesis. Melanoma generally shows as asymmetrical, unevenly bordered moles or black patches, with uneven pigmentation. Notably, melanoma may develop anywhere on the body and has a greater chance of spreading if not detected early [24].

2.1.2. Types of skin cancer

2.1.2.1. Non-melanoma skin cancer (NMSC)

Basal cell carcinoma (BCC) is the most prevalent kind of skin cancer globally, primarily affecting regions of the skin that are often exposed to sunlight. BCC is caused by the abnormal proliferation of basal cells in the skin's outermost layer and typically grows slowly. Figure 2.3 shows several clinical images of BCC. Most BCC instances are confined and have a low potential to spread, making them less dangerous than other skin cancers. However, if left untreated, it can penetrate neighboring tissues, causing substantial tissue damage [25,26]. BCC usually occurs in sun-exposed regions such as the face, neck, and hands, and is more commonly detected among individuals with fair skin [27].

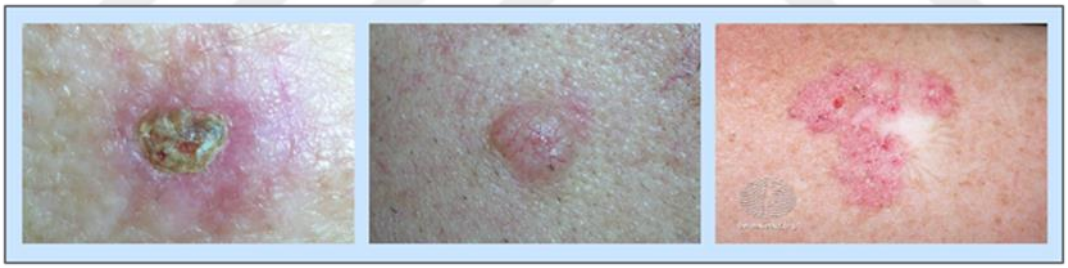

Figure 2.3. The clinical images of BCC [28,29]

BCC is normally diagnosed with a clinical examination and biopsy. Lesions frequently appear as pearly, elevated, and even ulcerated structures. Dermoscopy allows dermatologists to inspect lesions in greater detail [30]. Surgical excision, cauterization, cryotherapy, and topical medicines are some of the treatment strategies. Early detection of BCC leads to low recurrence rates and effective treatment [31,32]. However, surgical surgery for high-risk locations or severe BCCs may be more complicated and cause cosmetic scars. As a result, early identification and successful treatment of BCC is critical for patients' quality of life [33,34].

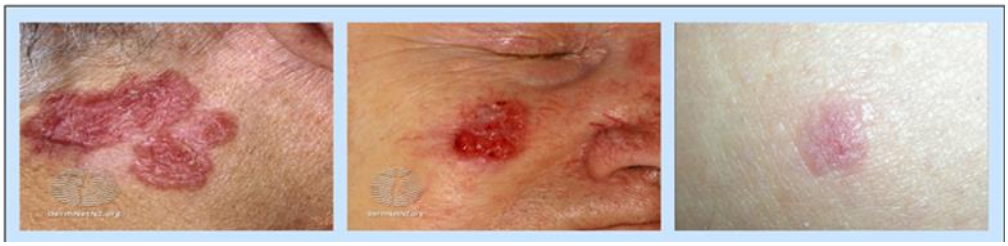

Figure 2.4. The clinical images of squamous SCC [29]

Squamous Cell Carcinoma (SCC) is the second most prevalent skin cancer after basal cell carcinoma, having the leading mortality rate among non-melanoma skin cancers [35-37]. Some example clinical images are shown in Figure 2.4. The occurrence of SCC is strongly linked to being exposed to ultraviolet radiation and sunlight; therefore, it often originates on persistently sun-exposed parts of the body, like the head or neck around 55% [38,39]. Other typical locations are the legs, shoulders and back. SCC, on the other hand, can appear anywhere, such as the lips, genitals and anus [40]. The clinical appearance of SCC is various, including plaques, papules, and nodules with silky, scaly, or ulcerated surfaces.

In the bulk of instances, actinic keratosis (AK) and squamous cell carcinoma in situ (SCCIS) or Bowen's disease are thought to be the precursor lesions of SCC, and patients are usually diagnosed with SCC in addition to multiple precursor lesions. Actinic keratoses are thought to represent the initial stage of squamous cell cancer. These keratoses, which are characterized as premalignant lesions, do not invariably proceed to cancer. By minimizing sun exposure, as much as 25% of actinic keratoses additionally referred to solar keratoses can decline [37]. The most typical sign of AK is a raised pink or red scaling plaque or papule on a sun-exposed area. Since it is difficult to predict whether AC may progress to SCC, the patient's condition is continuously monitored to avoid endangering the patient's life [41].

Obtaining independent morbidity and mortality statistics for BCC and SCC within NMSC data is difficult, owing to how these data are usually bundled in cancer registries. Yang et al. [42] studied keratinocyte skin cancer statistics across 33 countries and found that while SCC has a greater mortality than BCC, detailed tracking of these diseases is frequently confined to nations with high-quality cancer registries, such as Australia and the USA. In a comprehensive analysis, Wehner et al. [43] emphasized that SCC poses a larger risk of all-cause death than BCC, although the high incidence and relatively low lethality of NMSC overall sometimes led to BCC and SCC being recorded combined, confounding efforts to differentiate morbidity and mortality

data. Jensen et al.'s [44] cohort research in Denmark discovered that BCC was related with a lower risk of death, but SCC had a higher mortality rate, particularly among older people and those with comorbidities. The study indicated that while death rates varied between BCC and SCC, correctly separating these data points might be challenging because to confounding health variables influencing survival.

2.1.2.2. Melanoma

Melanoma is one of the most serious and aggressive kinds of skin cancer, and it develops from melanocytes, the cells that create melanin pigment. Melanoma, unlike other skin tumors, may spread swiftly to deeper skin layers, lymph nodes, and potentially other organs [45]. It is more frequent among those with pale skin and who have been exposed to a lot of sunshine. Exposure to the sun's ultraviolet (UV) radiation has been related to the development of melanoma, making sun protection essential in lowering melanoma risk [46]. Figure 2.5 shows several clinical images of melanoma.

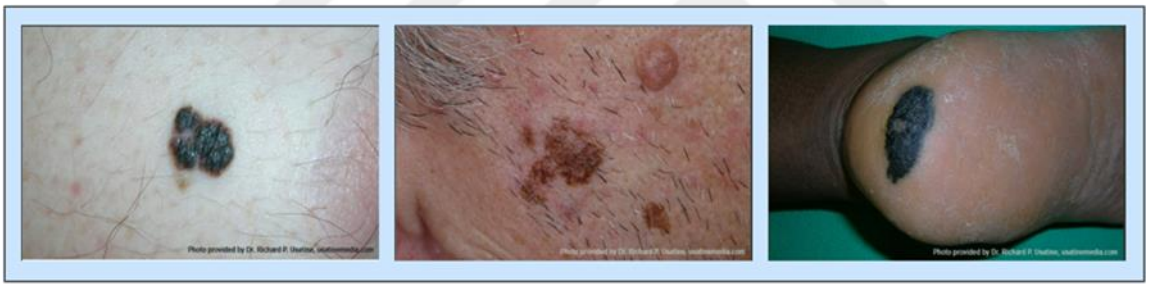

Figure 2.5. The clinical images of melanoma [29]

Melanoma symptoms may manifest as a change in the size, shape, or color of a mole. The "ABCDE" method is often employed in melanoma diagnosis: asymmetry, border irregularity, color variation, diameter, and evolving or changing lesion [47]. These markers assist in distinguishing between melanoma and benign moles, giving a valuable guideline for both patients and healthcare practitioners in spotting early warning symptoms. If these symptoms are present, a dermatological examination is necessary. Biopsy of suspicious lesions is the conventional procedure for determining a diagnosis. When identified early, melanoma can be entirely removed surgically, increasing the chances of effective therapy [48].

Among the types of skin cancer, melanoma has the highest fatality rate and is growing in prevalence globally. As reported by the World Health Organization (WHO), over 300,000 new

instances of melanoma are detected each year, with roughly 60,000 deaths. Melanoma is very prevalent in nations like Australia and New Zealand, where high UV radiation exposure and a generally fair-skinned population contribute [49]. While a high proportion of melanoma patients may be effectively treated if found early, survival chances decline considerably when metastasis occurs [50]. As a result, worldwide health systems are increasing their efforts to raise awareness about melanoma, create early detection programs, and promote preventative measures [51].

2.1.3. Diagnosis of skin cancer

Skin cancer has become a major public health problem because of increasing in both incidence and fatality rates. Melanoma is estimated to contribute considerably to these global trends. If current trends continue, predictions indicate a roughly 50% increase in melanoma cases and fatalities by 2040 [52]. Early detection is acknowledged as the most effective strategy in combating melanoma, as patients have a survival probability of over 90% when diagnosed at an early stage [53]. From a societal standpoint, advanced-stage therapies place a large fiscal burden on healthcare systems, stressing the necessity of early intervention [54].

Early diagnosis is key in minimizing the incidence of melanoma, thus both healthcare facilities and individuals play an important role. One of the most significant barriers to early detection is people's failure to consistently inspect lesions on their bodies. To overcome this, different ways have been developed to aid physicians and individuals in diagnosing melanoma, including instruments for self-examination to encourage proactive monitoring [55,56]. Figure 2.5 depicts a five-step strategy for carefully checking the skin, which is a generally suggested self-examination technique. This instruction shows how to evaluate the front and rear of the body, examine the arms, legs, and feet, and use a hand mirror to check hard-to-see places such the scalp, neck, and back. Regular self-examinations that follow these guidelines enable people to notice problematic lesions early and seek medical attention as soon as possible, which is critical for increasing melanoma survival rates.

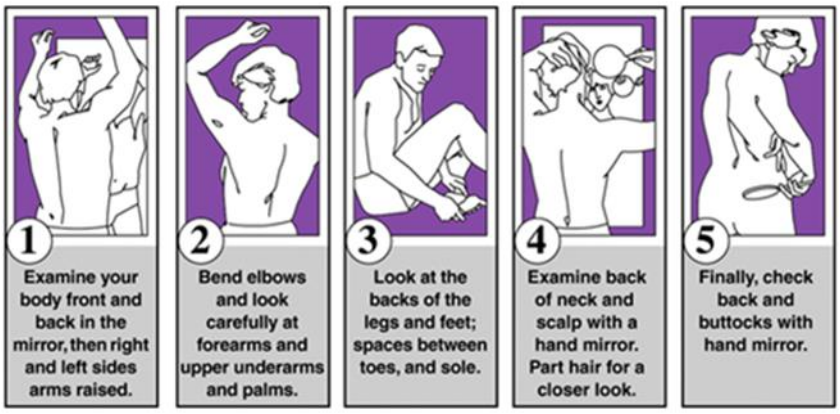

Figure 2.6. The steps for skin self-examination [57]

The ABCD criteria were introduced in 1985, which considerably increased public awareness of melanoma's early warning symptoms. These criteria—Asymmetry(A), Border irregularity (B), Color change (C), and Diameter (D) higher than 6 mm—were devised to differentiate between benign and malignant tumors based on typical melanoma features [56]. Later, the symbol “E” was added to point out on importance of evolution because melanomas frequently change size, color, or form over time. This ABCDE method has subsequently become a widely accepted technique for early melanoma identification [58].

Following a self-examination, it is critical to see an expert for a final diagnosis. Dermatologists use dermoscopy, a noninvasive diagnostic procedure that magnifies skin lesions in real time, allowing them to see subcutaneous abnormalities that are imperceptible to the human eye. A dermatoscope, sometimes known as a "skin microscope," comprises of a lens that magnifies at least tenfold, a light source, and a transparent plate, as shown in Figure 2.7, which illustrates a handheld dermatoscope [59]. In certain circumstances, a gel or oil is applied to the skin to reduce reflection and increase visibility of underlying structures by rendering the skin transparent. Certain dermatoscopes employ polarized light to decrease surface reflections, allowing for a speedier inspection without the need of gels or oils. However, for people with dry skin, these compounds may still be required for optimal results [60].

Figure 2.7. A hand-held dermatoscope [59]

Studies have shown that dermoscopy is a better diagnostic tool for identifying melanoma than naked eye inspection. According to research, dermoscopy is much more accurate in diagnosing melanoma than unassisted examination, particularly among dermatology-trained experts [61]. Additionally, another research has proven that dermoscopy is especially successful in distinguishing melanoma from other suspicious lesions [62]. However, it is crucial to emphasize that effective diagnosis of melanoma is dependent not only on the use of dermoscopy, but also on the physician's knowledge of the condition and familiarity with the equipment [63].

To improve diagnosis accuracy, computer-aided techniques have been designed to help doctors analyze pigmented skin lesions. These systems use cutting-edge algorithms and machine learning approaches to analyze dermoscopic pictures, detecting patterns and traits associated with both benign and malignant tumors. By evaluating massive datasets of tagged skin photos, these computers may discover minor traits that the human eye may miss, enhancing diagnosis accuracy. Computer-aided systems can be useful tools for physicians, allowing them to more accurately distinguish between benign and malignant tumors. When combined with a physician's experience, these technology technologies show promise for improving early detection and giving a more accurate and trustworthy diagnosis of melanoma [64,65].

2.2. Artificial Intelligence

Artificial intelligence (AI), the intelligence constituted by computer systems, creates, and analyzes methods that allow computers to utilize learning and intelligence to perform actions to reach specified objectives. AI, machine learning and deep learning interact with each other and constitute a hierarchical structure as illustrated in Figure 2.8. While AI offers a general structure, machine learning (ML) and deep learning (DL) apply this intelligence through learning from data.

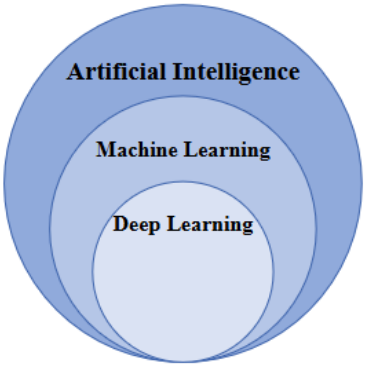

Figure 2.8. The relationship between artificial intelligence, machine learning and deep learning

In classical programming, results are achieved by processing the information in the data with external commands to the machine. On the contrary, ML, one of the sub-branches of AI, enables the machine to learn from data with various algorithms and generalize to reach the results. The comparison between classical programming and machine learning is illustrated in Figure 2.9. ML algorithms attempt to make the best predictions based on the data sets by extracting patterns. These algorithms rely heavily on their data sets. The more data they are trained on, the better they learn and the more accurate their predictions become.

As a subtype of machine learning, DL predicts output by learning from more complex data sets using artificial neural networks that operate on the same principles as neurons. These technologies have played a key role in numerous fields, ranging from early detection of terminal illnesses such as breast cancer, lung cancer, and COVID-19 to space applications like satellite image analysis, managing spacecraft, or monitoring potentially dangerous objects such as comets and asteroids [66-69].

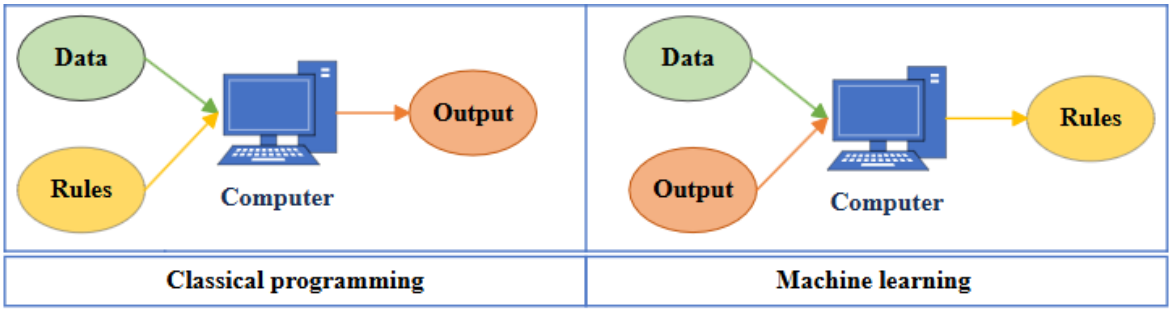

Figure 2.9. The comparison of classical programming and machine learning

2.2.1. Deep learning algorithms

2.2.1.1. Artificial neural network (ANN)

Deep learning is based on deep neural networks consisting of numerous layers with various neurons which are designed with inspiration from the biological neuron structure [70,71]. Neurons, which are illustrated in Figure 2.10, are the basic unit of the nervous system linking nerve cells to process and transmit electrical and chemical impulses in the human brain. Dendrites are branches taking input signals from other neurons. The cell nucleus processes the signals from the dendrites. Axon is employed by neurons to transmit information, and synapses operate as connectors between neurons [73].

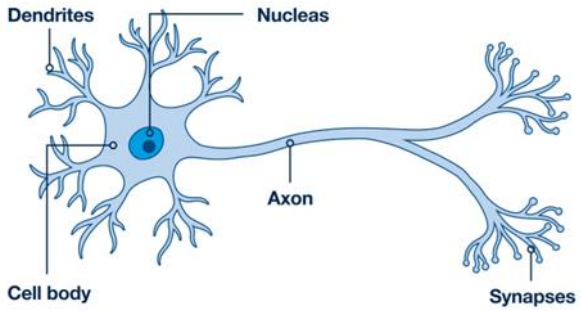

Figure 2.10. A single biological neuron structure [72]

Perceptron is an artificial neuron that uses calculations to identify features in input data. It is made up of output nodes entirely connected to a layer of input nodes. A perceptron is formed by key components that are input layer, weights, bias, activation function, summation function, and output as shown in Figure 2.11. The input layer has at least one node that accepts input signals. Each of the input nodes is related to a weight, which indicates the effectiveness of the

relationship between the input and output nodes. A bias, which is a constant value, is an additional input and has its own weight [74].

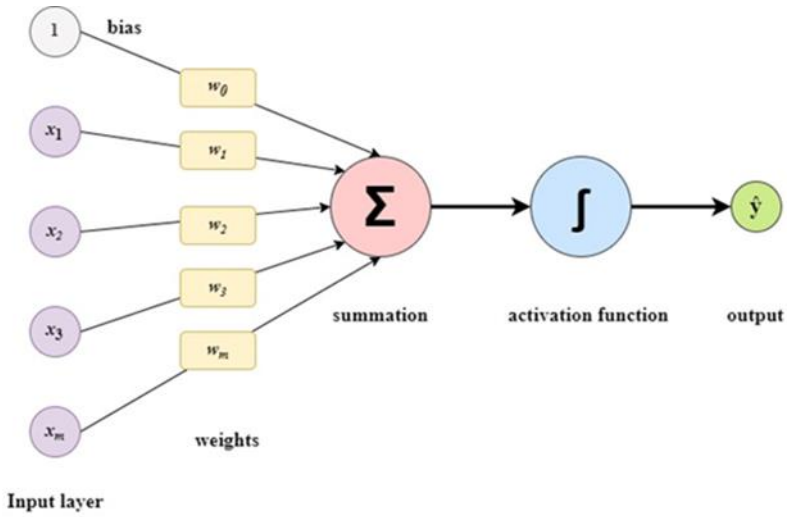

Figure 2.11. A perceptron structure

The mathematical representation of the perceptron is as in the following Equation 1. The values obtained by multiplying the inputs x_i with the weights w_i are summed, then bias w_0 is added and finally the result of applying the activation function g is obtained.

$$\hat{y} = g(w_0 + \sum_{i=1}^{m} x_i w_i) \quad (1)$$

An activation function determines whether to activate a neuron which means that it will employ basic mathematical calculations to decide if the input of the neuron is vital or not to the network throughout the prediction phase. It allows neural networks to learn and accomplish more challenging tasks by employing non-linear transformations. The details of the most used activation functions are given in Table 3.1 [74].

Many deep learning techniques are based on the underlying concept of artificial neural networks (ANNs), which are inspired by the structure and operation of the human brain [71,74]. ANNs are made up of linked processing units called neurons that are arranged in layers, allowing them to learn complex patterns and correlations in data [70,75]. An ANN is normally made up of three types of layers: the input layer, hidden layers, and output layer, as illustrated in Figure 2.12.

Table 2.1. The details of the most used activation functions

Activation function	Formula	Derivative	Graph
Sigmoid Function	$\sigma(x) = \frac{e^x}{e^x + 1}$	$\sigma'(x) = \sigma(x)(1 - \sigma(x))$	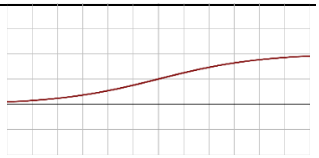
Tanh function	$\tanh(x) = \frac{e^x - e^{-x}}{e^x + e^{-x}}$	$\tanh'(x) = 1 - \tanh(x)$	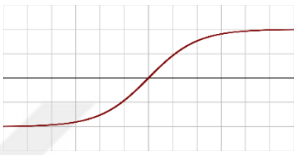
Rectified linear unit (ReLU)	$\begin{cases} 0 & if\ x \leq 0 \\ x & if\ x > 0 \end{cases}$	$\begin{cases} 0 & if\ x < 0 \\ x & if\ x > 0 \\ undefined & if\ x = 0 \end{cases}$	
Leaky rectified linear unit (Leaky ReLU)	$\begin{cases} 0.01 & if\ x \leq 0 \\ x & if\ x > 0 \end{cases}$	$\begin{cases} 0.01 & if\ x < 0 \\ 1 & if\ x > 0 \end{cases}$	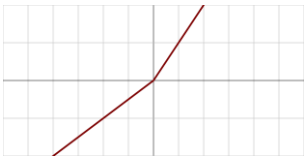

Depending of application, the input layers accept input data in a variety of formats, such as graphics, numerical data, or text. Each neuron in the layer represents a unique aspect of the input data, effectively preparing it for future processing [76]. The hidden layers positioned between the input and output layers perform complicated computations on incoming data. These layers extract characteristics, discover patterns, and convert the input into more advanced representations [71,75]. A neural network's number of hidden layers can vary greatly depending on the design needs; networks with a large number of hidden layers are referred to as deep neural networks (DNNs) [70]. Increasing the number of hidden layers improves the network's capacity to understand and solve complicated, nonlinear problems by collecting detailed patterns and correlations in the input [71,75].

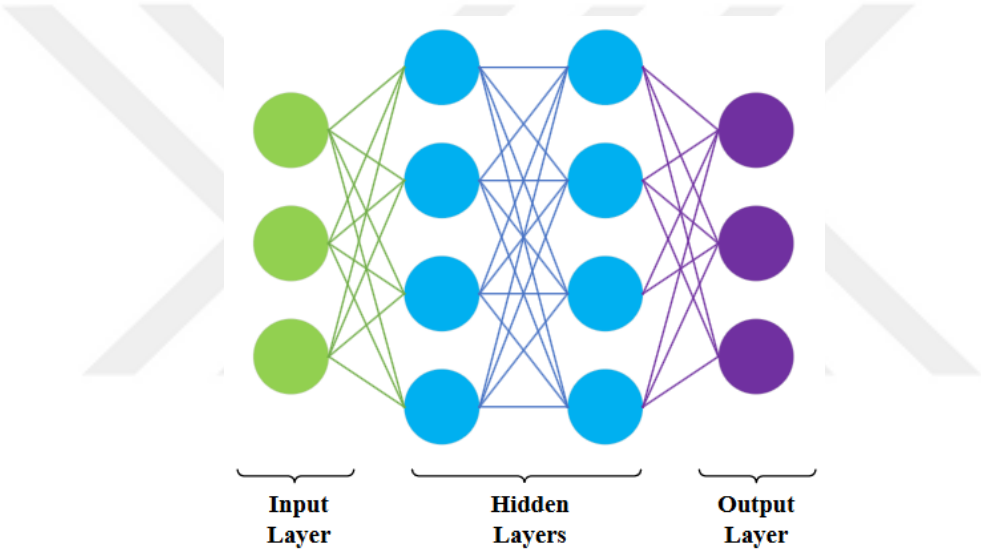

Figure 2.12. The layers of ANN

The output layer is in charge of creating the neural network's final output, which may be a classification, regression value, or any other required result depending on the job at hand. For example, in an image classification job, the output layer generates probabilities for each conceivable category, allowing the network to identify the most probable categorization for the input picture [76]. As the network trains, weights and biases inside the neurons are modified via an optimization method, allowing the model to increase its accuracy over time [70]. ANNs are excellent tools for a variety of applications, such as image identification, natural language processing, and predictive analytics, due to their versatility and ability to approximate complicated functions [71,74].

The learning process of ANN begins with taking inputs from the external world through the input layer to send data multiplied with some random weights to the hidden layers [71]. In the hidden layers, inputs are multiplied by their weights then a bias is added to provide an extra flexibility in simulating complicated patterns [70,74]. Afterwards, an activation function is employed to introduce non-linearity for learning non-linear, complicated relationships [71]. In the last step, we reach the output layer by passing through each hidden layer. This process, where inputs are multiplied by random weights from the input layer and then finished in the output layer, is called feedforward propagation as illustrated in Figure 2.13 [70].

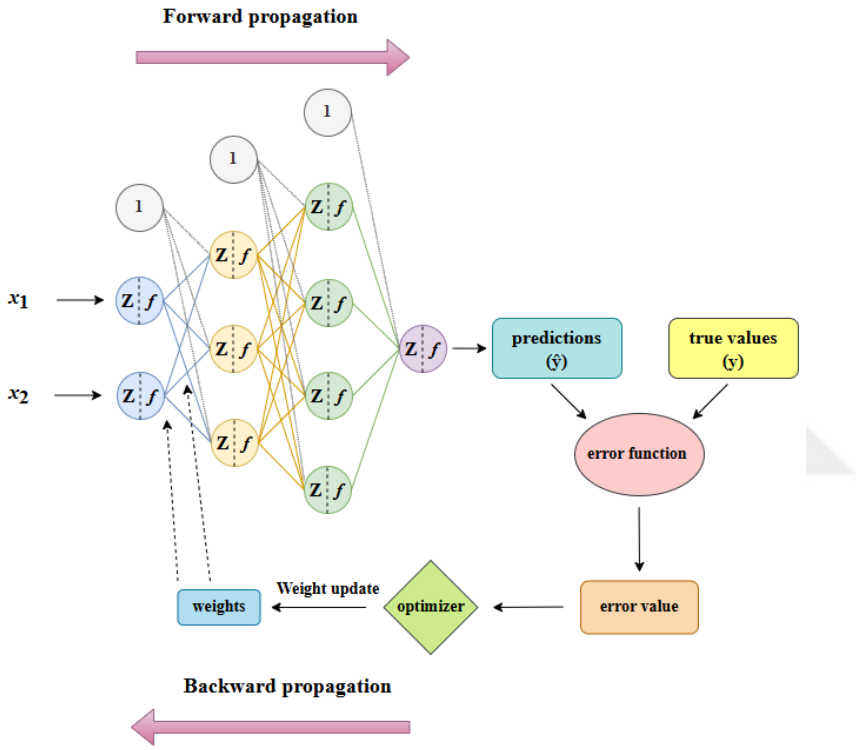

Figure 2.13. The illustration of forward propagation and backward propagation

Following receiving predictions from the output layer, the error is determined as the difference between the actual and expected output. It is utilized to modify the weights and biases of the network [77]. This process, which is iterative and entails going backward along the network, is called back propagation as presented in Figure 2.13 [71,77]. In this process, the optimal values of weights and biases are identified by updating them with the help of optimizers to minimize the difference between the actual and expected output [78].

2.2.1.2. Convolutional neural network (CNN)

Commonly viewed as a generalized neural cognitive machine, a CNN or ConvNet is a training network consisting of multiple single-layer convolutional neural networks including convolution, nonlinear transformation as well as downsampling, which is not mandatory for each layer. Due to their structure, CNNs are successfully employed in large-scale image feature tasks, such as object recognition and image classification [70,76].

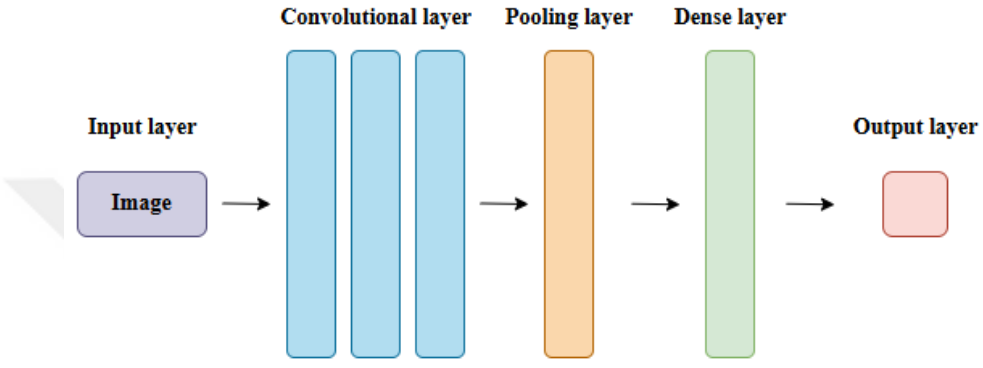

Figure 2.14. A simple CNN structure

A simple convolutional neural network is made up of numerous layers, including the input layer, the convolutional layer, the pooling layer, and the fully connected layer or dense layer as displayed in Figure 2.14 [71]. Layer inputs are feature maps composed of a set of vectors. When the input data is a digital image consisting of a grid-like arrangement of pixels with pixel values indicating how bright and which color it should be, the input layer can be represented by an n-dimensional matrix $I(x_n, y_n)$ where I is an intensity of the pixel with (x_n, y_n) position [78].

The convolution layer is the fundamental layer of a convnet, and its function is to extract features from the input image by employing convolution operation being displayed in Figure 2.15. This operation begins with accepting the input image. Then a two-dimensional array of weights which is called a filter or kernel is applied to a certain part of the image. A convolution layer consists of several filters that perform extracting different features such as vertical edges or horizontal edges. An element-wise multiplication is applied between the filter which is smaller than the input and the piece of the input image having the same size as the filter, then summed and produced a single value. As the filter or kernel shifts by several pixels which is called stride across the whole input image, an output array is obtained which is called feature

map or activation map being the input of the following layer. A feature map represents the response of the filter-sized portion of the input to the filter.

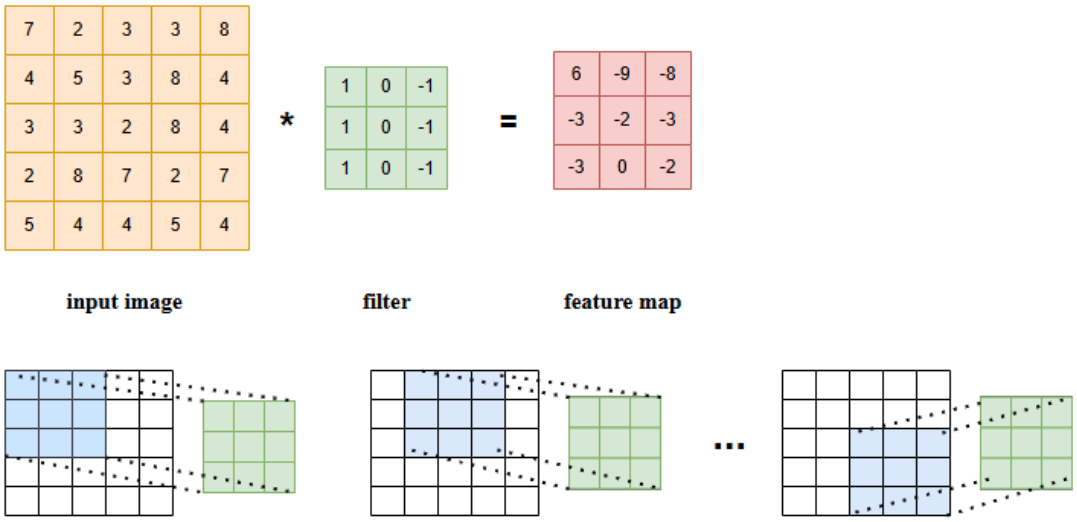

Figure 2.15. A convolution operation

During the convolution operation, the feature map is smaller than the input image and this reduction causes loss of edge information. To overcome this issue a technique called padding is employed. Padding is used to maintain the spatial dimensions of the input image by adding an extra layer of zeros around the feature map's border before the following convolution [71].

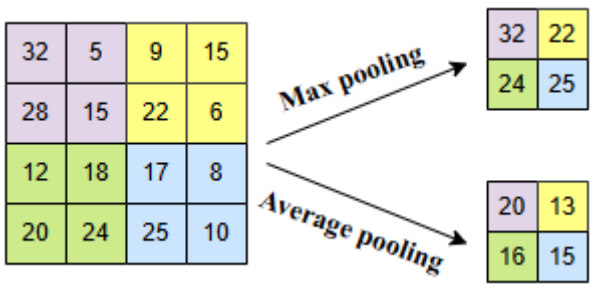

Figure 2.16. An example of pooling functions

Pooling layers reduce the size of the feature maps obtained by the convolutional layers; hence, it decreases both the quantity of features to learn and the amount of computation. In this layer, a filter size and a stride value are selected then this filter is applied to the feature maps. There are two types of pooling: maximum (max) pooling and average pooling. If the largest number in the area that is covered by filter in the feature map is chosen, this procedure is called max

pooling. If the average value of the elements in the filter-sized part of the feature map is calculated, it is called average pooling. These pooling functions are demonstrated in Figure 2.16 [78].

2.2.2. Types of CNN algorithms

Since their discovery, CNN algorithms have undergone continuous development. Sophistication has brought about different variants throughout time, most of which are specialized for solving specific problems in visual data processing. Some of those variants are simple and focus on fundamental image categorization, while others are more sophisticated and tackle more complicated tasks, such as object detection, semantic segmentation etc.

Some of those sophisticated varieties are LeNet [79], AlexNet [76], VGGNet [80], ResNet [81], and DenseNet [82]. Each with its own designs and innovations to improve performance, accuracy, and efficiency, these CNN variants differ in depth, structure, and layer connectivity allowing them to tackle more complicated tasks. Understanding the structure of the algorithm is critical for determining the best architecture for a given application, since each type provides different benefits depending on its design principles and performance characteristics.

LeNet-5, being accepted as one of the pioneer CNN architectures, was developed in 1990s by Lecun et. al. [79]. This network was created primarily to detect handwritten digits, a critical job in early ML applications such as automatic reading of zip codes on mail or recognizing numbers on bank checks. LeNet-5's design was groundbreaking at the time, introducing numerous features that are now common in current deep learning models.

The architecture is made up of three convolutional layers that extract characteristics from input pictures using filters to capture spatial hierarchies in the data. These convolutional layers are separated by two pooling layers, which minimize the spatial dimensions of the data, minimizing processing needs and assisting in the prevention of overfitting. Following the feature extraction layers are two fully linked (dense) layers that integrate the characteristics learnt by the preceding layers, allowing the network to make more complicated judgments. The last layer employs a Softmax classifier, which assigns probabilities to each output class, allowing the network to categorize the input picture into one of many groups.

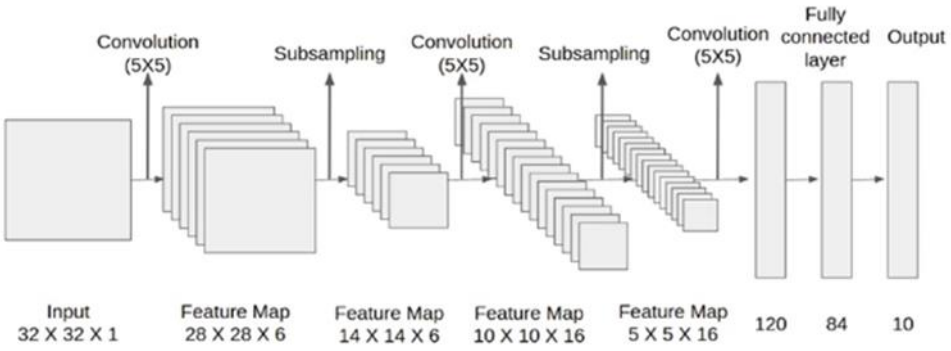

Figure 2.17. LeNet-5 model [83]

Figure 2.17 shows how LeNet-5's hierarchical structure allows it to learn representations of increasing complexity, beginning with simple edges and shapes in the early levels and progressing to more detailed characteristics in the deeper layers. Despite its simplicity by today's standards, LeNet-5 was a game-changing model that revealed CNNs' promise for image identification tasks and lay the framework for the creation of more advanced CNN architectures in following years. Its architectural concepts continue to impact current neural network models, demonstrating its historical relevance in DL.

Following the pioneering LeNet-5 architecture, which revealed CNNs' promise for image identification applications, AlexNet represented a significant advancement in the area. AlexNet, introduced by Krizhevsky et al. [76], won the ImageNet Large Scale Visual Recognition Challenge (ILSVRC) in 2012, establishing a new benchmark for DL performance in visual recognition. Unlike earlier models, AlexNet was the first design to completely utilize GPUs, dramatically increasing training performance and making it possible to train much bigger networks on enormous datasets.

AlexNet's architecture consists of five convolutional layers, three pooling layers, two normalization layers, and two fully connected (dense) layers, all followed by a Softmax classifier. It uses the ReLU activation function in all layers except the output layer, which speeds up training by addressing gradient vanishing difficulties. To boost training accuracy, data augmentation techniques were used to provide more diverse input data, allowing the network to generalize better. AlexNet also included convolution layers with varied kernel sizes, such as 3x3, 5x5, and 11x11, to capture different levels of spatial information. Furthermore, dropout layers were used to avoid overfitting, which is a typical problem in deep networks.

AlexNet's design, as seen in Figure 2.18., provides a considerable improvement over older models such as LeNet-5 and lays the groundwork for future improvements in deep convolutional networks.

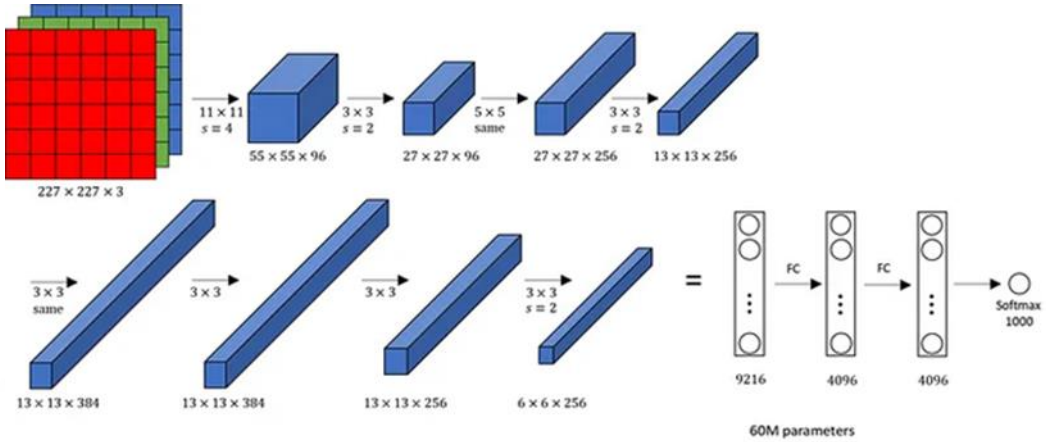

Figure 2.18. AlexNet model [84]

The Visual Geometry Group (VGG) at Oxford University introduced VGGNet [80], which builds on the success of prior CNN designs such as AlexNet and brings more innovation to DL in image categorization. VGGNet comes in numerous versions, including VGG16 and VGG19, each defined by the number of layers, which allow the network to learn more complicated and subtle patterns. This architecture primarily uses 3x3 convolutional layers layered on top of each other to boost network depth, allowing for the learning of complicated patterns while being simple in design.

One of VGGNet's main advantages is that its generalizability is improved by reducing overfitting during training through tiny convolutional layers. Notwithstanding its ease of use and excellent performance, VGGNet is more computationally intensive than its predecessors, requiring more memory and computing power. Because of its ability to balance accuracy and design clarity, the VGG16 architecture which is shown in Figure 2.19 remains popular in a variety of image classification applications.

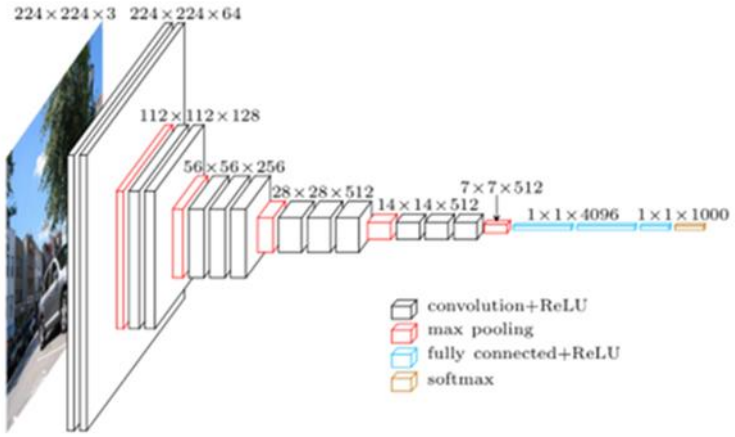

Figure 2.19. VGG16 network architecture [85]

In the 2014 ImageNet Large-Scale Visual Recognition Challenge (ILSVRC14), GoogleNet, also known as Inception v1 [86], adopted a different strategy after the significant debut of VGGNet, which illustrated the potential of deep networks with stacked tiny convolutional layers. The "inception module," a unique component created by Google researchers, distinguished its design from earlier CNN models. The inception module uses different-sized kernels, including 1x1, 3x3, and 5x5, to create many convolutional layers that are organized in parallel. While the various filter sizes facilitate feature extraction at various scales, this parallel structure enables the network to capture more thorough information, improving the model's capacity to recognize intricate patterns.

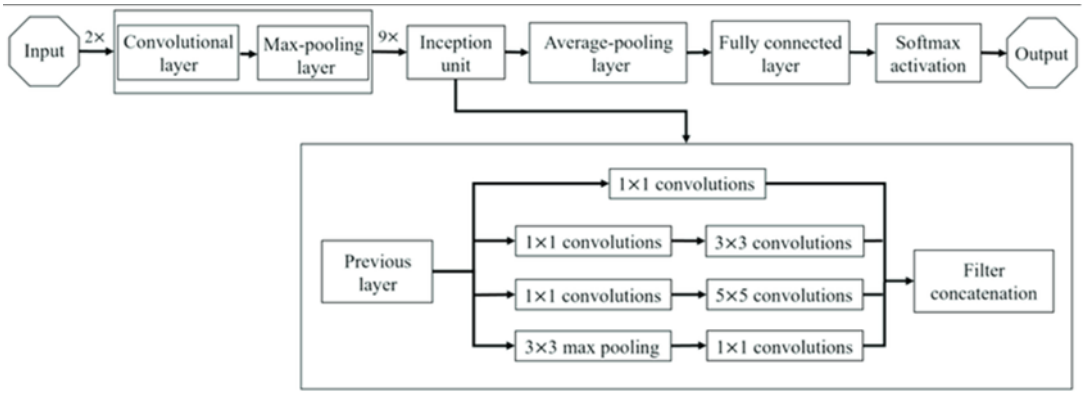

Figure 2.20. A simplified illustration of GoogleNet [87]

Remarkably, GoogleNet uses fewer parameters than its predecessors to reach a depth of 27 layers, or 22 if pooling levels are removed. In contrast to VGG and AlexNet, GoogleNet often uses 1x1 convolutional layers to minimize the dimensionality of feature maps. This reduces the

number of parameters and computational load without sacrificing important information. Figure 2.20 provides a simplified representation of the GoogleNet architecture, highlighting its distinctive and effective design that signaled a shift in CNN topologies.

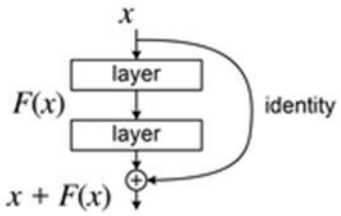

Figure 2.21. A Residual Block in a deep Residual Network [88]

In 2015, Microsoft researchers created ResNet (Residual Network) [81] , which built on the advancements made by GoogleNet. ResNet tackled the "vanishing gradient" problem, a significant DL obstacle that can impede the training of extremely deep networks. ResNet overcame the issue by introducing "residual connections" or skip connections, which enable data to slip through specific layers and enter subsequent layers directly as illustrated in Figure 2.22. This method made it possible to create much deeper networks without sacrificing training effectiveness, which resulted in a significant improvement in performance on challenging image recognition tests. The topology of ResNet, shown in Figure 2.21, established a new benchmark for CNN architecture by enabling the training of models with hundreds or even thousands of layers.

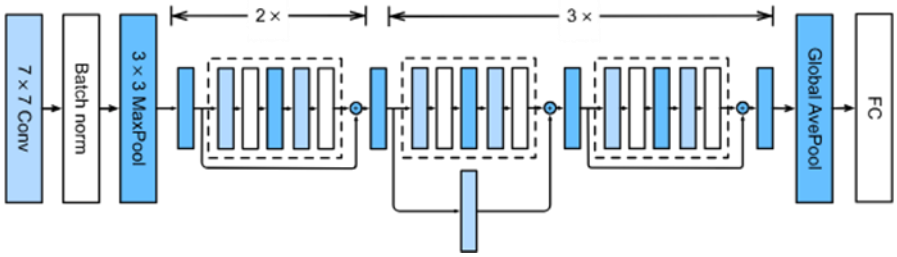

Figure 2.22. The ResNet-18 architecture [89]

DenseNet (Densely Connected Network) [82], which was released in 2017, further developed the idea of layer connection after ResNet. To ensure that every layer obtains the accumulated knowledge from all previous layers, DenseNet uses dense connections between each layer and every other layer. Compared to conventional deep networks, DenseNet's architecture greatly

minimizes the number of parameters and enables effective feature reuse, making it both computationally economical and powerful. As illustrated in Figure 2.23, DenseNet's architecture makes use of dense connections to enable the model to learn intricate features with fewer resources, leading to excellent performance on a variety of computer vision applications.

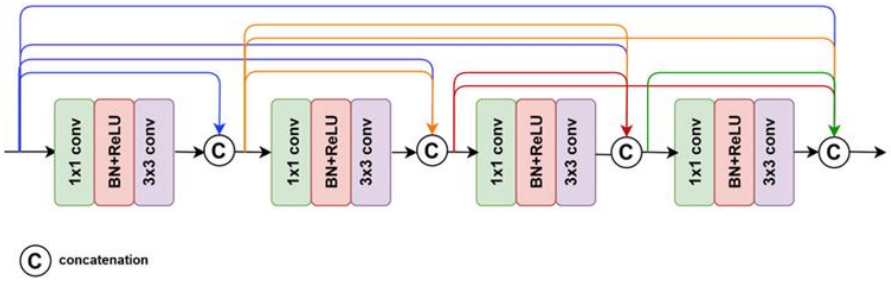

Figure 2.23. The basic architecture of DenseNet [90]

Extreme Inception, or shortly, Xception is a DL model developed by François Chollet at Google [91]. Unlike standard CNN models, its architecture is entirely based on depth-separable convolutional layers, shown in Figure 2.24. That is to say, Inception modules are replaced by depthwise separable convolutions in CNN architecture.

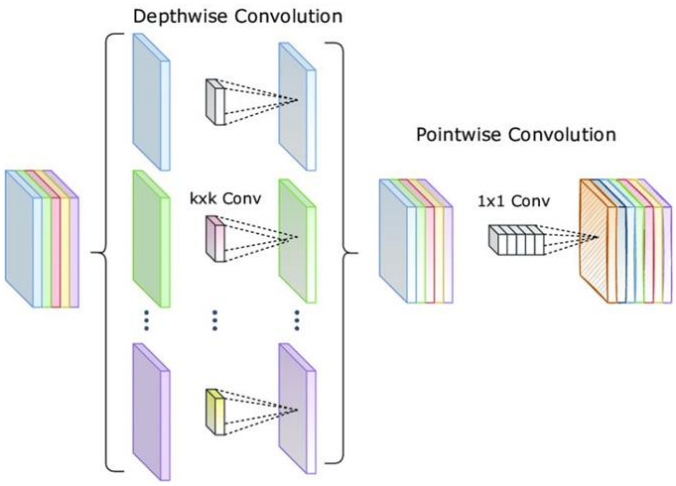

Figure 2.24. Depthwise separable convolution [92]

The Xception model is an advanced model that relies on fundamental elements from Google's Inception architecture and has a similar parameter count as Inception_V3 [93] , while providing a more streamlined and efficient framework.

Unlike standard convolutions, Xception uses depthwise separable convolution that streamlines the convolution process by dividing it into two phases.The first phase is depthwise convolution, which processes each channel individually and extracts spatial information on a per-channel basis. The second phase, pointwise convolution, uses 1x1 filters to aggregate all channels, allowing the model to learn cross-channel correlations. This architecture not only lowers processing costs but also minimizes the number of parameters, allowing for faster and more effective feature extraction.

In this study, dermoscopic images from the HAM10000 [94] dataset are classified as malign benign using the Xception model combined with transfer learning.

2.3. Datasets

Using a variety of datasets and DL techniques, research on the early detection of skin cancer has advanced significantly. In addition to serving as a significant source of data for DL model training, the datasets utilized in skin cancer diagnosis are essential for increasing diagnostic precision. Melanoma, basal cell carcinoma, and other skin lesions are among the many photos in the ISIC (International Skin Imaging Collaboration) dataset [95], which is one of the most popular datasets in the literature. Figure 2.25. displays a selection of images from the ISIC archive, demonstrating the range of lesion types and imaging quality in the collection. By hosting yearly competitions, the ISIC dataset makes it easier to create increasingly complex models and is regarded as a standard benchmark in the industry.

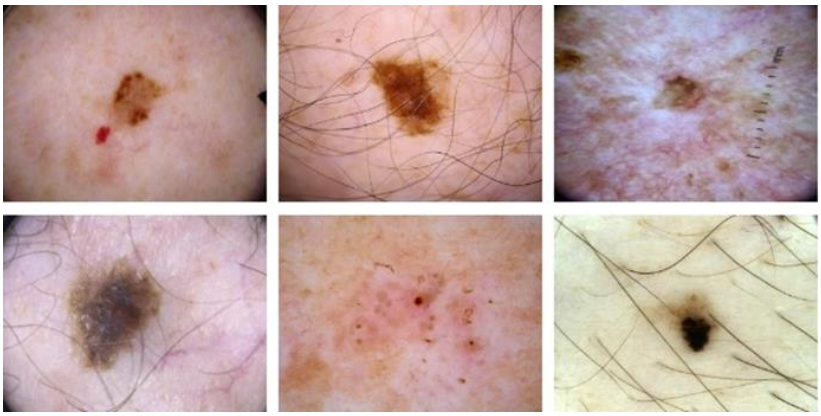

Figure 2.25. A selection of images from the ISIC archive [95]

With roughly 10,000 photos of skin lesions, HAM10000 (Human Against Machine with 10,000 training images) [94] is another crucial dataset that is used in skin cancer classification research. The inclusion of seven distinct skin lesion types in HAM10000 enables a thorough assessment of models' capacity to carry out intricate classifications that go beyond merely differentiating between benign and malignant lesions. Melanoma, basal cell carcinoma, and actinic keratosis are among the lesion types found in the HAM10000 dataset; these include both common and uncommon skin disorders. Because of this diversity, DL models created for the diagnosis of skin cancer can be extensively trained, improving their appropriateness for practical uses. A selection of sample photos from the HAM10000 dataset are shown in Figure 2.26., which highlights the dataset's diverse and rich structure.

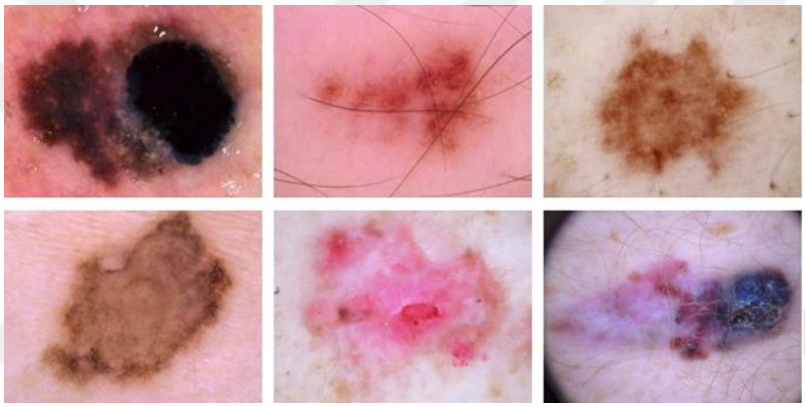

Figure 2.26. A selection of images from HAM10000 [94]

Other prominent datasets for skin cancer diagnosis include PH2 [96], Derm7pt [97], and BCN20000 [98]. The PH2 dataset focuses on melanoma diagnosis and includes approximately 200 dermoscopic pictures categorized as malignant or benign. This dataset is extremely important for scientists looking to create models capable of high-accuracy categorization. The Derm7pt dataset, on the other hand, distinguishes itself by categorizing dermoscopic pictures using seven separate criteria, enabling model training that mirrors clinicians' actual diagnostic procedures.

The BCN20000 dataset [98], which contains roughly 20,000 dermoscopic pictures, is one of the largest datasets that includes a wide range of skin lesions. BCN20000, which includes both uncommon and common skin lesions, is used to assess a model's ability to categorize lesions across a broad range. These datasets enable researchers constructing DL models for skin cancer

diagnosis with a large and diverse data set, improving model accuracy and allowing for comparison study.

These datasets are critical in assessing the performance and improving the accuracy of DL models designed for skin cancer diagnosis. Several researchers have used these datasets to produce effective outcomes in skin cancer categorization. DL-based models, in particular, are commonly used to classify skin lesions with high accuracy. Deep neural network designs such as ResNet [81], DenseNet [82], and Inception [86], for example, have produced impressive results in the classification of melanoma and other skin diseases. Because of the variety in these datasets, these designs go through a more thorough training process, making them more successful in real-world applications. In addition, research has used transfer learning techniques and data augmentation strategies to increase model performance. As a result, DL approaches are becoming more effective instruments for diagnosing skin cancer.

Studies in this topic show how different DL architectures and approaches have been used to diagnose skin cancer. Numerous research in the literature has confirmed that DL models can correctly categorize and diagnose skin lesions. For example, Osman et al. [99] the efficient MobileNet V2 model to diagnose skin lesions in the HAM10000 dataset, with an accuracy of 98.5%. This lightweight CNN architecture was chosen for its applicability for mobile applications, since it combines great performance with efficient resource use.

Mehr and Ameri [100] performed research using the Inception-ResNet-v2 model, a complex DL architecture that combines both Inception and ResNet layers to maximize the characteristics of each technique. This model was first pretrained in object identification tasks, which allowed it to use past knowledge in picture processing. To increase diagnosis accuracy, the scientists included additional metadata such as lesion location, patient age, and gender giving the model context beyond only the lesion's visual features.

Imran et al. [101] studied to improve model accuracy in skin lesion categorization by using regularization approaches and fine-tuning hyperparameters. They built a six-layer proprietary convolutional neural network (CNN) model on the HAM10000 dataset, which is a popular dataset for skin lesion pictures. Regularization techniques, such as dropout or weight decay, were used to keep the model from overfitting, which is a typical problem with DL models and can lead to poor generalization on fresh data. Furthermore, hyperparameter tweaking lets the

authors adjust variables such as learning rate and batch size for improved performance. Using these strategies, the model's accuracy increased to 88%, effectively addressing the greater misclassification rates reported in earlier models.

Singh et al. [102] used transfer learning approaches to enhance skin cancer diagnosis with convolutional neural network (CNN) models, notably VGG-16, MobileNet, and InceptionV3. They were able to use transfer learning to use pretrained models that already contained learned feature representations from huge picture datasets, hence improving feature extraction in the skin cancer classification challenge. This method minimized the requirement for substantial training from scratch while improving model performance. Also, they created a web application for real-time skin cancer diagnosis in order to make their work more practical and accessible. This tool allows users to effortlessly upload photos for rapid analysis, making it suitable for both clinical and individual use. The work emphasizes the potential of transfer learning paired with CNN architectures for practical, accessible skin cancer diagnostics, acting as a link between advanced machine learning techniques and real-world healthcare applications.

Obaid et al. [103] used the HAM10000 dataset, containing 10,015 annotated images of various skin conditions, to investigate the categorization of skin lesions. They used the Keras Sequential API to create a CNN model and compared its performance to other transfer learning models including ResNet50, DenseNet121, and VGG11. They used a variety of data preparation approaches, including data augmentation, to increase model dependability. This strategy enabled the model to attain an astounding 97.12% accuracy in discriminating between different types of skin lesions, proving the efficacy of both their CNN model and the comparative transfer learning models in skin cancer detection.

Amin et al. [104] intend to enhance skin cancer diagnosis by integrating two key tasks: location and categorization of skin lesions using DL. The authors describe deep feature fusion, a strategy for combining information from many neural network layers to provide a more detailed depiction of skin lesions. Localization defines the precise region of interest (ROI), allowing the model to concentrate on the lesion itself, whereas classification classifies the lesion as benign or malignant, facilitating early diagnosis and treatment planning. By combining data from lower and deeper levels, where lower layers capture basic visual information and deeper layers recognize complicated lesion-specific patterns, the model improves accuracy in both tasks. The model, which is most likely based on convolutional neural networks (CNNs), benefits from a

large dataset like HAM10000 or ISIC, which are routinely used in skin lesion investigations. This technique has the potential to help dermatologists make more exact diagnoses and might be modified for use in mobile or computer-aided diagnostic systems, hence increasing early diagnosis availability.

Majtner et al. [105] study the use of an ensemble of convolutional neural networks (CNNs) to improve the classification accuracy of dermoscopic pictures for skin cancer diagnosis. Dermoscopic pictures, which provide precise views of skin lesions, are suitable for automated analysis, notably for identifying melanoma and other skin malignancies. The study attempts to improve the accuracy and resilience of diagnosing skin lesions by using ensemble learning, which mixes numerous CNN models rather than depending on a single one. Ensemble approaches take advantage of the distinct capabilities of several CNNs, such as ResNet, Inception, VGG, and DenseNet, allowing each model to focus on different aspects of the pictures. This variability allows the ensemble technique to discriminate between benign and malignant tumors more accurately, reducing the likelihood of misclassification. The work uses data augmentation strategies to increase model generalization, most likely employing huge datasets such as ISIC or HAM10000. This ensemble technique overcomes issues such as visual resemblance between benign and malignant tumors, resulting in higher classification accuracy. Clinically, this strategy may benefit dermatologists by offering trustworthy second views and perhaps eliminating the need for invasive biopsies. Furthermore, it has the potential to be integrated into computer-aided diagnostic tools, which would improve skin cancer screening accessibility and accuracy.

Thurnhofer-Hemsi et al. [106] presented a novel hierarchical classification method for skin cancer diagnosis in 2021, departing from typical single-network techniques. Instead of depending on a single deep network, they created a two-level categorization system using two neural network models to improve diagnosis accuracy. At the most fundamental level, the first network model separates nevi (moles) from other skin lesions, successfully excluding benign instances. The second network then divides the remaining lesions into six distinct groups, allowing for a more precise and nuanced diagnosis. The model was pre-trained on the ImageNet dataset and then tuned on the HAM10000 dataset to provide resilience and reliability in real-world applications. The results showed that DenseNet201 outperformed other deep networks, improving performance indicators like sensitivity and specificity by about 10%. This novel two-

tiered technique not only promotes more exact skin cancer categorization, but it also has the potential for implementation in clinical situations where high accuracy and quick decision-making are critical.

Using the ISIC 2018 dataset [107], Gouda et al. [108] created a computer-based approach for accurately detecting and diagnosing benign and malignant skin lesions. To improve picture quality during the preprocessing step, the study used ESRGAN (Enhanced Super Resolution Generative Adversarial Networks), which sharpened lesion borders and increased contrast, allowing for more detailed feature extraction. Data augmentation techniques including resizing, rotation, and brightness modifications were then used to improve data variability and model resilience. The suggested architecture employed a transfer learning technique to investigate four neural network models: CNN, ResNet50, Inception V3, and a hybrid ResNet50-Inception model. Inception V3 had the best accuracy, about 86%, and beat other designs in identifying skin lesions.

Skin cancer detection research is getting more diversified and complex, with the use of multiple datasets, DL architectures, and improved image processing approaches. These research seek to increase diagnosis accuracy by using various machine learning models and DL algorithms to reliably categorize skin lesions. Numerous research has been conducted to assess the performance of popular models including as ResNet, Inception, and DenseNet, as well as architectures backed by transfer learning, data augmentation, and high- resolution picture enhancement techniques for skin cancer diagnosis. Table 2.2. summarizes these investigations, including the datasets, architectures, and performance metrics attained.

Table 2.2. Summary of some studies on skin cancer detection

Study	Dataset	Model	Methods	Accuracy
Nida et al. [109]	ISIC-2016	region-based Convolutional Neural Networks (R-CNNs)	RCNN for localization and Fuzzy C-Means (FCM) clustering for segmentation	94.8%
Alwakid et al. [110]	HAM10000	modified ResNet-50, modified CNN	ESRGAN for image enhancement,data augmentation	86%
DeVries et al. [111]	ISIC dataset	a multi-scale CNN approach	Transfer learning with Inception-v3	90%
Shorfuzzaman [112]	ISIC	an explainable CNN-based stacked ensemble framework	three CNN sub-models with fine-tuned weights called DenseNet121, Xception, and EfficientNetB0	95.8%
Ogundokun et al. [113]	Kaggle dataset	a hybrid deep convolutional neural network architecture	Concatenation of MobileNet and Xception Models	97.6%
Rashid et al. [114]	ISIC 2020	MobileNetV2	Transfer learning with MobileNetV2	98.2 %
Mehmood et al. [115]	HAM10000	a modified Xception model	reducing the depth and expanding the breadth of the Xception architecture	97%
Das et al. [116]	HAM10000	a complex deep neural network	Inception-ResNet- V2	98.7%
Ahmad et al. [117]	PH2, ISIC, HAM10000	Vision Transformer (ViT)	ViT model for classification and DeepLabv3+ for lesion segmentation	100%
Wei et al. [118]	ISBI 2016	MobileNet and DenseNet	pre-trained lightweight network as a feature extractor	96%

3. METHODOLOGY

Skin cancer is the most common type of cancer, and its diagnosis is a critical concern in dermatology, with serious implications for public health. Detecting skin cancer involves identifying and diagnosing malignant skin lesions using a range of methods, including visual examination, dermoscopic imaging, and advanced technologies like machine learning and DL. These technologies hold considerable potential to improve the efficacy and accuracy of skin cancer diagnosis [119].

Computer-aided skin cancer diagnosis systems show promising results in detecting cancerous lesions at early stages. These systems analyze images of benign and malignant skin lesions using specialized algorithms. However, such images often contain unwanted artifacts, such as light reflections, air bubbles, ruler lines, and hair, which complicate diagnosis and reduce the accuracy and efficiency of detection systems [120-122].

Hair, a natural occurrence on human skin, is one of the main challenges for these systems, and various solutions have been proposed to address this issue. The first method in this area, known as Dullrazor [123], is an algorithm designed to detect and remove hair from dermoscopic images to enhance image quality and facilitate more accurate analysis of skin diseases. In this approach, a generalized grayscale morphological closing operation is applied separately to each color band (red, green, and blue) using three different kernel orientations. A thresholding method then creates a binary hair mask, and the bilinear interpolation technique replaces hair pixels with neighboring non-hair pixel values. Finally, a median filter smooths the image while preserving fine details, improving the image quality for further examination.

Xie et al. [124] proposed another method to remove hair from dermoscopic images. This method consists of three phases. In the first phase, the hairs of malignant lesion are improved via utilizing morphologic closing-based top-hat operator and a probability- based threshold approach is used to create binary hair images. In the second phase, hair pixel values are obtained by connected region elongation and in the last phase PDE-based image inpainting procedure is employed to restore hair-occluded information resulting in effective separation of hairs from the surrounding skin.

Kiani et al. [125] presented a new method which comprises identifying hair pixels with edge detection techniques, replacing them with non-hair pixels, finally smoothing the skin lesion image for eliminating both light and dark hairs from dermoscopic images. In this study, four distinct edge detection techniques which are Prewitt Filter, Sobel Filter, Laplacian Operator and Laplacian of Gaussian Operator are compared to find out which one is the most successful at spotting hairs in dermoscopic images. The Prewitt filter showed the best capability of recognizing hairs in terms of signal-to-noise ratio (SNR). This filter had a higher SNR, indicating that it performed more efficiently in recognizing hair pixels properly while reducing the identification of non-hair pixels. In comparison to Dullrazor algorithm, this algorithm is more successful in terms of eliminating both dark and light-colored hairs and also has a faster processing time.

Another hair segmentation procedure is implemented by Huang et al. [126]. In this study, a multiscale matched filtering procedure is suggested to recognize tiny hairs or hairs in shadowy areas that the Dullrazor [123] method cannot detect successfully. Moreover, region-growing approaches from adjacent identified hair sections, combined with LDA (linear discriminant analysis) based on a color similarity specification, are suggested to restore the complicated hair intersection structures.

In this study, some filters have been developed to address this issue. The aim of these filters is not only to remove hairs from the images but also to ensure that they can be used in the preprocess section of skin cancer diagnosis with DL algorithms without damaging the structure of the lesion in the image. In this study five different filters were applied to the public dataset HAM10000 [94], two of which were developed in our previous work [127]. Their performance in diagnosing skin cancer using artificial intelligence was compared with that of the Dullrazor filter and a filter developed based on the Blackhat technique.

3.1. The Hair Removal Filters Used in This Study

3.1.1. Dullrazor (F1)

The Dullrazor filter is recognized in the literature as the first proposed solution for the issue of hair removal in images. This filter’s design consists of three main steps: first, identifying the locations of hairs in the image; second, removing the hair pixels and filling the empty spaces

using the values of neighboring non-hair pixels; and finally, smoothing the edges of these filled areas.

To detect the hairs' locations, the filter applies grayscale morphological closing with kernels oriented in different directions. The identified hair pixels are then filled by bilinear interpolation using the values of nearby non-hair pixels. Finally, the boundaries of these filled regions are smoothed using an adaptive median filter. The following Figure 3.1 shows the workflow diagram along with the before-and-after effects of Dullrazor application. This filter, being economical and easy to implement, has proven effective in detecting dark-colored hairs in images. However, it has been observed that the filter's effectiveness decreases in areas with dense hair or when detecting fine hairs, as illustrated in Figure 3.1. Subsequent studies in this field have sought to address these limitations.

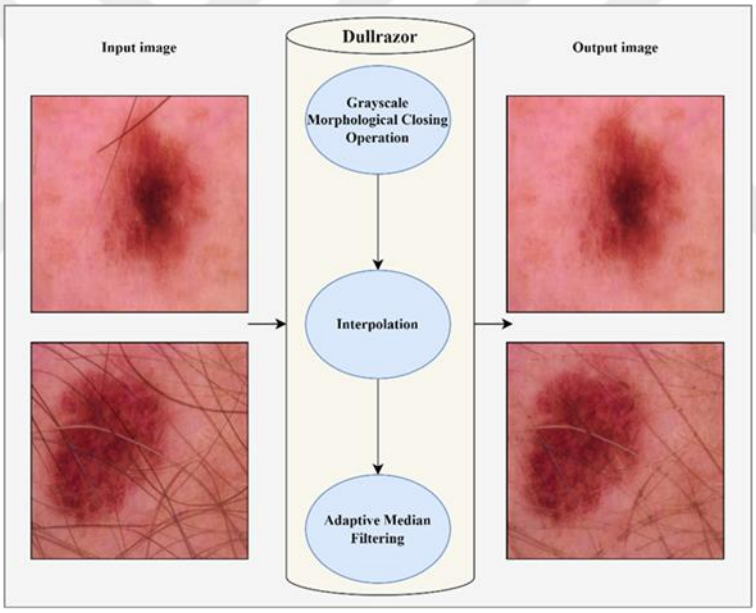

Figure 3.1. The workflow of Dullrazor and its application

3.1.2. Blackhat based filter (F2)

This filter was designed to improve the accuracy of skin cancer diagnosis system [128]. In this filter, Blackhat transformation was used for hair detection, followed by binary thresholding to create hair masks. These masks were then filled in using inpainting techniques with the pixel values of non-hair areas. After this, the images were smoothed using a median filter. The method, as illustrated in figure 3.2. below, was found to clean hairs more effectively compared

to the Dullrazor technique. However, it was also observed that the lesion structures in the images were prone to distortion.

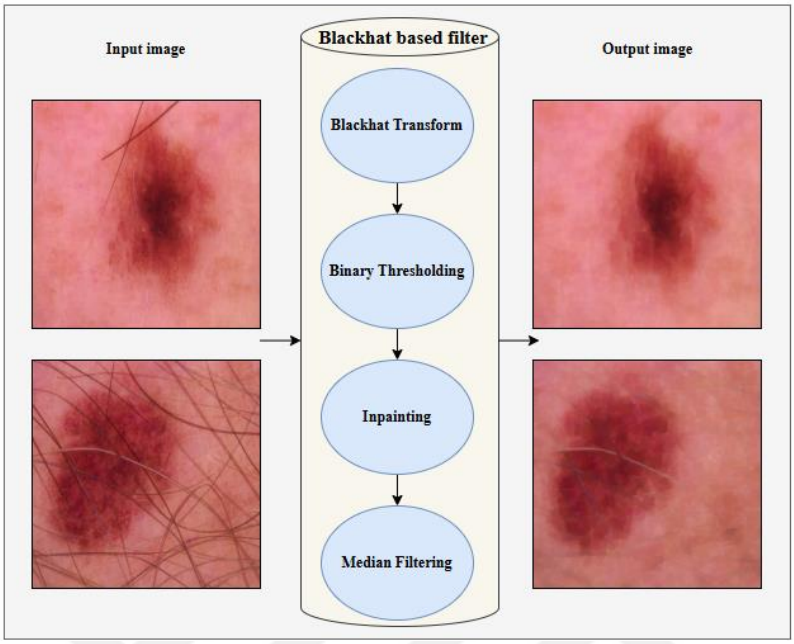

Figure 3.2. The workflow of the filter and its application

3.2. The Hair Removal Filters Developed in This Study

3.2.1. Blackhat-based hair removal filters (F3)

In this study, additional steps were incorporated into the filter used in our previous research. To remove noise from the image to be processed, the Wiener filter was applied. Developed by Austrian mathematician Norbert Wiener [129], the Wiener filter is widely used in signal and image processing. This filter seeks to reduce noise from a noisy signal or image, aiming to approximate the undistorted signal or image as accurately as possible by considering the statistical characteristics of a noise-corrupted signal or image. Wiener filtering is a mathematical approach to noise removal. When working with continuous time signals or images, the filter's fundamental equations can be represented in various forms. The core equation of the Wiener filter can be expressed in the frequency domain using the Fourier transform. The objective of this filter is to minimize the mean square error between the filtered and original signals, ensuring the filtered signal is as close as possible to the original. Wiener filter, a H(f) is defined as the transfer function and is expressed as

$$H(f) = \frac{S_{xy}(f)}{S_{xx}(f)} \quad (2)$$

In Equation 2, $H(f)$ indicates transfer function of the Wiener filter, $S_{xy}(f)$ is cross-spectral density of the observed (noisy) signal and the original signal, $S_{xx}(f)$ shows power spectral density of the original signal.

Wiener filter works with minimum squared error estimation and the estimated signal $\hat{x}(t)$ is in obtained as

$$\hat{x}(t) = \sum_k h(k)y(t-k) \tag{3}$$

In Equation 3, $\hat{x}(t)$ is the estimated signal, $y(t)$ is the observed signal that contains noise, $h(k)$ is the impulse response of the Wiener filter and *t* is time variable, also *k* is an index related to the time delay in the filtering process. This equation estimates the signal by combining observable signal $y(t)$ with weighted impulse response $h(k)$ across time.

In order to find the location of hairs, the denoised digital lesion pictures are transformed using the Blackhat algorithm [130]. This algorithm is a morphological procedure that results in highlighting darker objects than the surrounding area. The image formed by the difference between the morphological closure of an image and the original version of this image is the Blackhat transformation of the original image. Its mathematical equation is given in Equation 4 below.

$$T_b(f) = f o\ b - f \tag{4}$$

In Equation 4, f represents the original picture, b represents the structure element, and "$\circ$" is the morphological closure operator. The characteristics of the structural element are chosen based on the objects to be detected during the Blackhat transformation.

The image produced by the Blackhat transform is subtracted from the grayscale image generated by the Wiener filter, followed by applying the contrast-limited adaptive histogram equalization (CLAHE) method to enhance hair visibility further. This image enhancement technique, widely used in medical imaging, involves dividing the image into homogeneous, non-overlapping subregions. The histograms of these subregions are calculated, and interpolation is applied to smooth any inconsistencies at the boundaries of the subregions [131].

Thresholding, a commonly used image processing method, creates a mask of the desired object in the image. Pixels below the set threshold are changed to black, while those above are

converted to white. In this study, it was found that the global thresholding method was insufficient for producing an accurate binary hair mask. In global thresholding methods, a single threshold value is applied to the entire image. In contrast, adaptive thresholding calculates a unique threshold for each point in the image, based on specific characteristics of neighboring pixels. Here, the adaptive mean thresholding method was used to obtain binary hair images [132]. Mathematically, this can be expressed as:

$$T(x,y) = \frac{1}{N}\sum_{i,j\epsilon S(x,y)} I(i,j) - C \quad (5)$$

This can be expressed by calculating the threshold *T(x,y)* for each pixel at location *(x,y)* as the average intensity of pixels in its neighborhood. *S(x,y)* adjusted by subtracting a constant *C*. *I(i,j)* represents the intensity values of pixels within the neighborhood, N is the total number of pixels in that neighborhood, and *C* is a constant that fine-tunes the threshold by shifting it relative to the local mean. This method produces a binary image by classifying each pixel as hair or non-hair based on whether its intensity exceeds this locally computed, adjusted threshold.

After that, the Median filter [133], a popular approach in image processing, was used for reducing noise, notably salt-and-pepper noise. In contrast to linear filters, that can blur edges, the median filter adjusts each pixel's value with the median of nearby pixel values within a specified frame, such as 3x3 or 5x5 pixels. This approach helps to retain the integrity of essential image characteristics, making it useful for applications that need edge preservation, such as medical imaging and computer vision. Mathematically, it can be described as:

$$I'(i,j) = median\{I(i+m, j+n) \mid (m,n) \in W\} \quad (6)$$

For a pixel located at position (i,j) in an image I, the median-filtered value, indicated as $I'(i,j)$,is determined by taking the median of all pixel values $I(i+m, j+n)$ within a neighborhood window W centered around (i,j).

In this study, image inpainting is used to restore hair pixels in images. The purpose of inpainting is to fill missing or damaged areas so that the reconstruction appears natural and blends seamlessly with the surrounding content. Different algorithms exist for inpainting, such as diffusion-based inpainting, where neighboring pixel values are diffused into the missing region; exemplar-based inpainting, where missing areas are filled by copying patches from undamaged neighboring areas; and DL-based inpainting, which uses large datasets to predict and fill

missing areas. The TELEA inpainting algorithm, also known as the Fast-Marching Method (FMM) [134], is used to restore hair pixels. This algorithm fills missing or damaged portions by iteratively propagating pixel values from known regions into the target area using a rapid marching process. It leverages information from neighboring pixels to recreate missing sections smoothly, prioritizing pixels with greater certainty, which effectively fills small gaps. The Telea method propagates known pixel information from the boundaries of the missing (or masked) region toward its interior, controlled by the image's gradients to ensure a seamless connection between the inpainted region and the surrounding area. Mathematically, the Telea inpainting algorithm can be summarized as follows:

$$I(x,y) = \frac{\sum W(x,y) \cdot I(x',y') . G(i,j)}{\sum W(x,y) . G(i,j)} \tag{7}$$

In this context, $I(x,y)$ represents the intensity value of the pixel being filled at location (x,y), while $W(x,y)$ denotes the local neighborhood around this pixel that provides the necessary information for inpainting. The intensity values of neighboring pixels within $W(x,y)$ are represented by $I(i,j)$, and $G(i,j)$ is a weight function based on both the pixel's distance and gradient, which prioritizes pixels with higher certainty. This approach enables the algorithm to propagate the most reliable pixel information into missing areas, ensuring a smooth transition between the restored region and its surroundings.

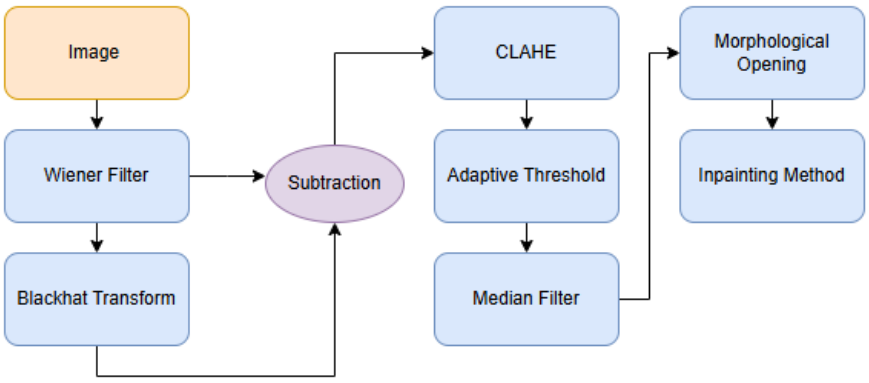

Figure 3.3. The steps of designed Blackhat based hair removal filter

This filter performs effectively in removing dark hair from lighter-colored skin backgrounds, making it particularly useful for certain skin tones and hair contrasts. This effectiveness in high-contrast situations allows the filter to cleanly differentiate and remove hair without disturbing

the surrounding tissue. However, in scenarios where the hair is finer or lighter in color, or where the hair and skin tones are closer in color, additional adjustments or alternative methods may still be necessary for optimal results. Figure 3.4 shows the application of the designed Blackhat-based hair removal filter. Overall, while this filter addresses some of the limitations observed in Dullrazor, such as skin texture preservation, it faces similar challenges with dense hair coverage, indicating an area for future improvement in hair removal techniques for skin lesion images.

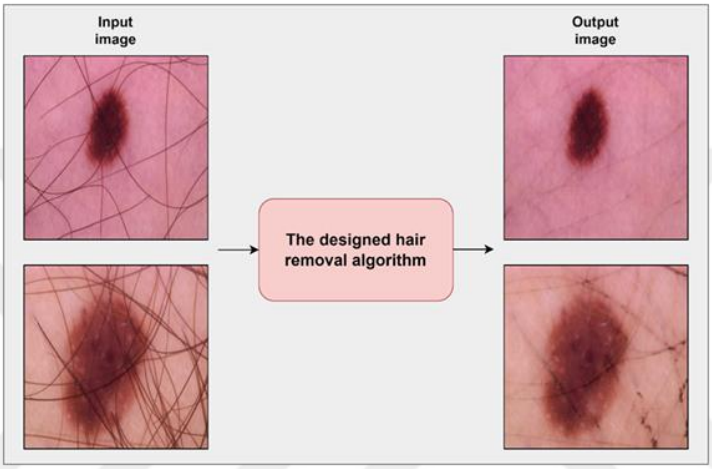

Figure 3.4. The application of designed blackhat based hair removal filter

3.2.2. LoG based hair removal filter (F4)

This filter resembles the designed Blackhat-based hair removal filter, with the primary difference being the method used for hair detection as shown in Figure 3.5. Here, the Laplacian of Gaussian (LoG) is employed to locate hair pixels in the skin lesion image. LoG is a two-step image processing technique commonly used for edge detection [135]. It combines Gaussian smoothing [136], which reduces noise, with the Laplacian operator. Applying Gaussian smoothing first, noise that could lead to false edges in the detection phase is minimized. The Gaussian function, used for this smoothing, is defined as follows:

$$G(x,y) = \frac{1}{2\pi\sigma^2} exp\left(-\frac{x^2+y^2}{2\sigma^2}\right) \quad (8)$$

where x and y represent coordinates of the pixel and σ is the standard deviation of the Gaussian distribution, controlling the amount of smoothing applied. In this approach, the Gaussian filter blurs the image to suppress noise, and then the Laplacian operator is applied to highlight the

edges, including hair pixels. This method enhances the detection of hair structures in the image while reducing artefacts caused by noise, ultimately improving the accuracy of hair pixel localization.

The Laplacian is a second-order derivative function that calculates the rate at which the image's gradient changes, focusing on areas with rapid intensity shifts, which are likely to correspond to edges. In two dimensions, the Laplacian operator can be defined as:

$$\nabla^2 I(x,y) = \frac{\partial^2 I(x,y)}{\partial x^2} + \frac{\partial^2 I(x,y)}{\partial y^2} \tag{9}$$

where ∇^2 is the Laplacian operator, and $I(x,y)$ is the image intensity at the point (x,y). The first term represents the second partial derivative of $I(x,y)$ concerning the *x* coordinate, while the second term is the second partial derivative for the *y* coordinate.

The Laplacian of Gaussian (LoG) operator is obtained by applying the Laplacian operator to the result of Gaussian smoothing. This combined approach helps reduce noise before edge detection. Mathematically, the LoG operation is represented as:

$$LoG(x,y) = \nabla^2[G(x,y) * I(x,y)] \tag{10}$$

where $*$ denotes the convolution operation, $G(x,y)$ is the Gaussian kernel, and $I(x,y)$ is the input image. This operation first smooths the image using Gaussian filtering, which reduces noise, and then applies the Laplacian operator to highlight areas of rapid intensity change, effectively detecting hair pixels in the image.

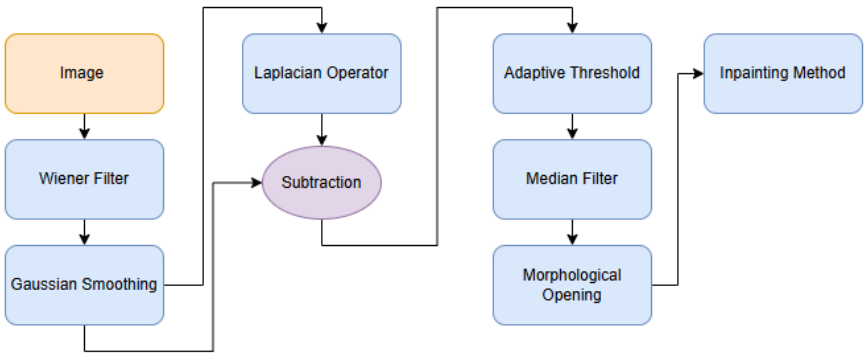

Figure 3.5. The working principle of LoG based filter

While the filter achieves noticeable hair reduction, it does cause slight alterations to the skin texture around the lesion in Figure 3.6. This minor texture disruption, visible in the output, is less pronounced than in some other hair removal methods, but it indicates that the LoG-based algorithm may not entirely preserve the lesion's natural appearance. Despite this limitation, the filter is still a valuable tool for reducing hair obstructions, particularly in images where dark hairs obscure the lesion, although further refinement may be needed to minimize texture impact fully.

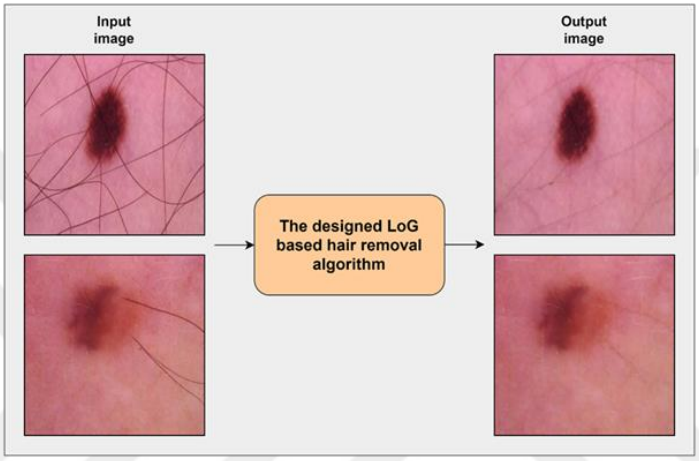

Figure 3.6. The application of LoG based hair removal filter

3.2.3. A hair removal filter using the blackhat transform based on the red channel (F5)

A digital image consists of a grid-like arrangement of pixels with pixel values indicating how bright and which color it should be. It is represented by a n-dimensional matrix such as $I(x, y)$ where I indicate the pixel intensity and (x, y) denotes the coordinates of the pixel in the image [136]. A color image is a digital image that includes color information for every pixel, for example, an RGB (red, green, blue) image. An RGB image consists of three main color channels: red, green, and blue. Each color channel has values, which are typically in a range from 0 to 255, indicating the intensity of that specific color. Many colors can be produced by integrating these three channels. Figure 3.7 displays an RGB image presentation.

Figure 3.7. An RGB image and its presentation to a computer

This method introduces some differences compared to the initial approach developed. In this method, the image is first divided into four equal sections. Each section is then separated into its RGB channels. The Blackhat operation is applied specifically to the red channel using four different directional kernels to enhance hair detection. The result from the Blackhat operation is then subtracted from the blue channel to improve hair visibility.

Following this, similar to the first designed filter, an adaptive thresholding technique is used to create a hair mask. Unlike the initial filter, a morphological dilation operation is incorporated here to expand the detected hair regions slightly. This dilation step enhances the effectiveness of the mask by ensuring that the entire hair structure is captured, including finer strands that may have been missed initially. This mask enables the cleaning of hairs in the image by repainting those regions. Finally, the four processed sections are merged to reconstruct the full image. The steps of this filter are illustrated in Figure 3.8, while the final result after applying the filter is shown in Figure 3.9.

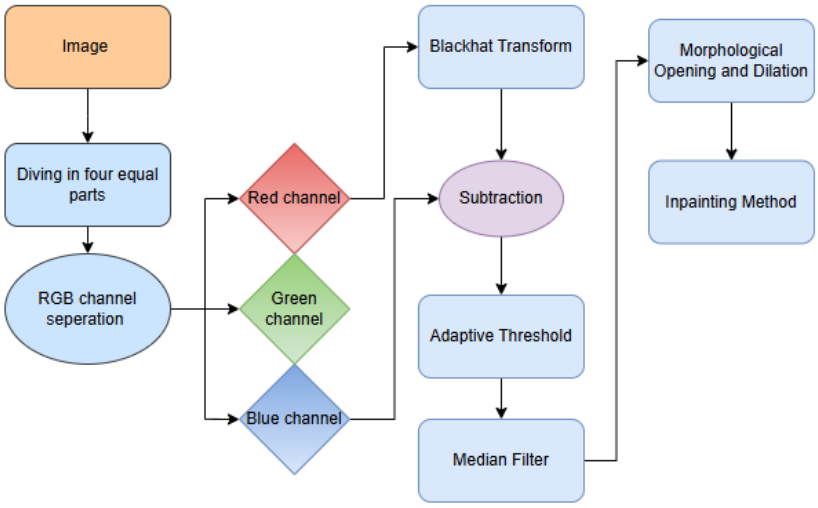

Figure 3.8. The steps of hair removal filter

The figure 3.9. illustrates the application of the designed hair removal algorithm on skin lesion images. The input images on the left show skin lesions obscured by fine, scattered hairs. After processing with the algorithm, the output images on the right reveal clearer views of the lesions with much of the hair removed. This algorithm successfully reduces hair visibility, especially for lighter and finer hairs. While it effectively cleans the majority of hairs, it is evident that some finer hair artefacts remain, particularly in more complex areas of the lesion. However, the algorithm's approach preserves the overall structure of the lesion without introducing significant artefacts or distortions.

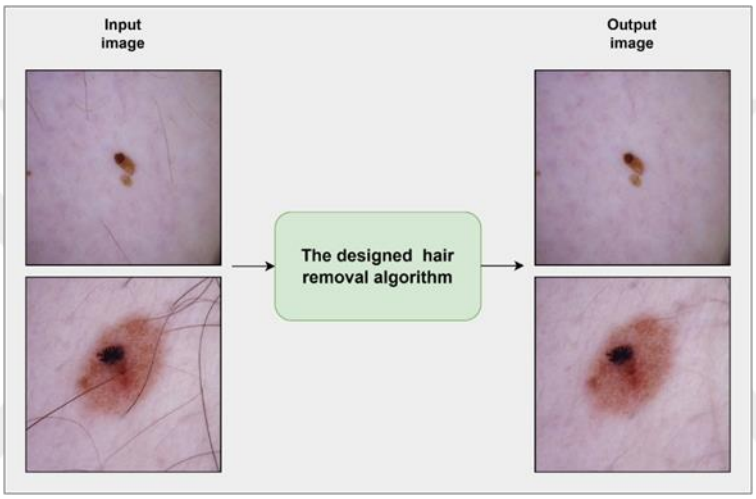

Figure 3.9. The application of F5 hair removal filter

In this study, a comprehensive graphical user interface (GUI) was developed, as illustrated in Figure 3.10, to enable a detailed comparative analysis of various hair removal filters used in dermoscopy images. This tool integrates filters previously applied in research, specifically F1 and F2, alongside newly developed filters F3, F4, and F5. The GUI allows for the automatic application of these filters to lesion images, offering users the flexibility to visually evaluate each option and select the most effective filter for each case. The F1 filter, commonly known as "Dullrazor," is an external software tool developed for Windows that has been integrated into the application to provide seamless accessibility. In contrast, filters F2, F3, F4, and F5 were implemented directly within the program using Python, leveraging image processing libraries such as OpenCV and Skimage to ensure adaptability and efficiency.

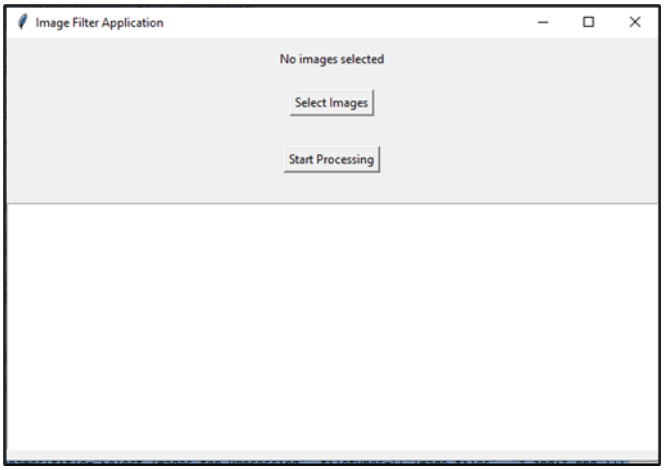

Figure 3.10. GUI for hair removal filters in dermoscopy images

Each filter applies a unique approach to hair removal, combining various image processing techniques. The F1 filter employs a standard hair removal method, while F2 introduces an adaptive thresholding technique to create a hair mask, followed by morphological dilation to expand the detected hair regions slightly. This dilation step enhances the mask's coverage, ensuring more comprehensive hair removal. The other filters, F3, F4, and F5, build on these foundational techniques, incorporating additional methods for contrast enhancement, morphological operations, and inpainting to optimize hair removal in different scenarios.

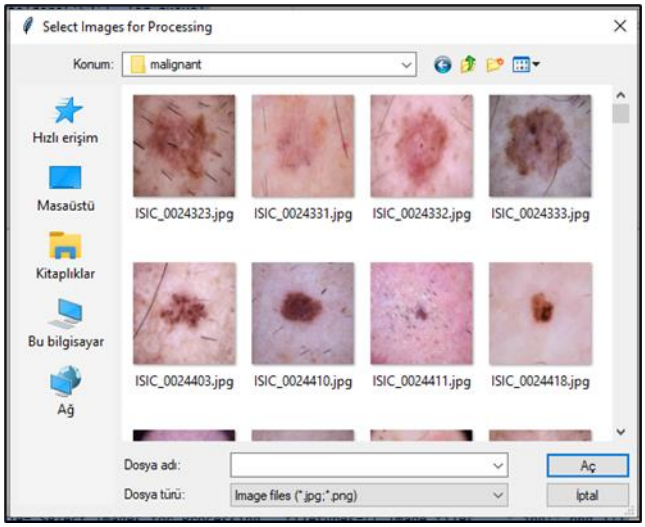

Figure 3.11. Image Selection Screen in the GUI

Additionally, the GUI features an intuitive image selection screen, as shown in Figure 3.11, which enables users to easily browse and select dermoscopy images for analysis. This screen

allows for smooth navigation through the local file system to find desired lesion images, which are then automatically loaded into the application. Users can preview selected images before applying filters, ensuring they make the right choice, and they can also select multiple images at once for simultaneous processing.

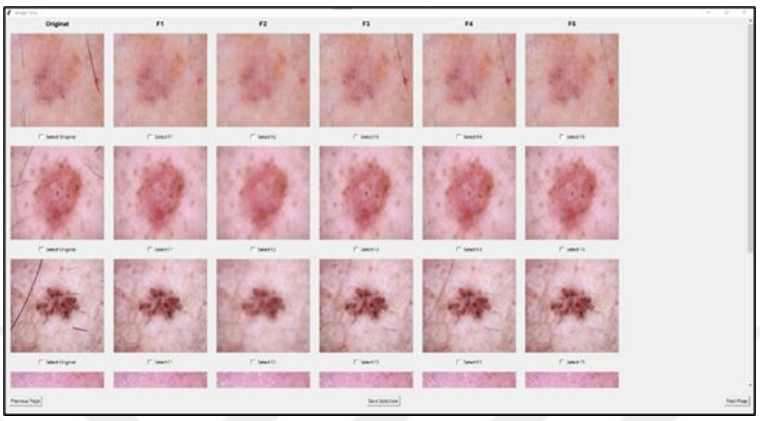

Figure 3.12. Side-by-side comparison of original and filtered dermoscopy image

As shown in Figure 3.12, the interface presents each original image alongside five filtered versions, enabling users to directly compare the effectiveness of each filter in hair removal. This side-by-side visual assessment capability is key in selecting the most appropriate filter for optimal lesion analysis. Furthermore, as depicted in Figure 3.13, the application allows users to save their filter selections in an Excel file, systematically storing these choices to support consistent data collection for further analysis.

	A	B	C	D	E	F	G
1	**Orijinal Resim Adı**	**Orijinal**	**F1**	**F2**	**F3**	**F4**	**F5**
2	ISIC_0024418.jpg	0	1	0	0	0	0
3	ISIC_0024450.jpg	0	0	0	1	0	0
4	ISIC_0024463.jpg	0	1	0	1	1	0
5	ISIC_0024522.jpg	0	1	0	0	0	0
6	ISIC_0024562.jpg	0	1	0	0	0	0
7	ISIC_0024575.jpg	0	1	0	1	1	0
8	ISIC_0024800.jpg	0	1	0	0	0	0
9	ISIC_0024925.jpg	0	1	0	1	1	0
10	ISIC_0024948.jpg	0	1	0	1	0	0
11	ISIC_0025069.jpg	0	1	0	1	1	0
12	ISIC_0025089.jpg	1	1	0	1	0	0

Figure 3.13. Excel export function for filter selection and data collection

4. RESULTS AND DISCUSSION

Hair removal is an important preprocessing step to provide reliable findings in skin cancer detection. Hairs on the skin's surface might conceal the structure of the lesion and generate visual noise, making it difficult for the model to interpret the lesion accurately. This visual noise can interfere with segmentation and classification operations, since the algorithm may incorrectly detect hairs as part of the lesion. Hair removal produces a cleaner, noise-free picture, allowing the model to concentrate entirely on the real details of the lesion.

To improve the accuracy and reliability of artificial intelligence algorithms in skin cancer diagnosis, five different filters were applied to skin lesion images containing hair artifacts from the HAM10000 dataset, and their impacts on the diagnostic process were investigated. In this study, we processed a total of 1,554 images of these 780 malignant, while the remaining 774 are benign using five different hair removal filters.

Data augmentation techniques including rotation, shifting, zooming, and horizontal flipping are used to increase the model's performance and capacity to generalize over a wide range of data patterns. A 5-fold cross-validation approach is used to divide the data into various groups, allowing the model's performance to be evaluated over numerous data subsets while minimizing variations and delivering a more robust performance measurement.

For classification, the Xception model is pre-trained using ImageNet weights, allowing for faster and more effective learning, particularly on a small dataset. As part of the model refining phase, the final ten layers of the Xception model are unfrozen, allowing them to be fine-tuned for skin lesion characteristics. While the pre-trained layers offer a solid basis of generic features, fine-tuning the final few layers allows the model to capture domain-specific patterns, hence improving classification performance. Additional layers, such as global average pooling and dropout layers, are added to decrease overfitting and increase model generalization. The final layer is dense, with a sigmoid activation function allowing binary categorization of benign and malignant tumors.

During training, the model leverages the Adam optimizer with a modest learning rate and the Early Stopping method to end training when no further develops in validation loss are noticed,

hence conserving the optimal model weight. The accuracy results are examined to determine the performance of hair removal filters on skin cancer classification.

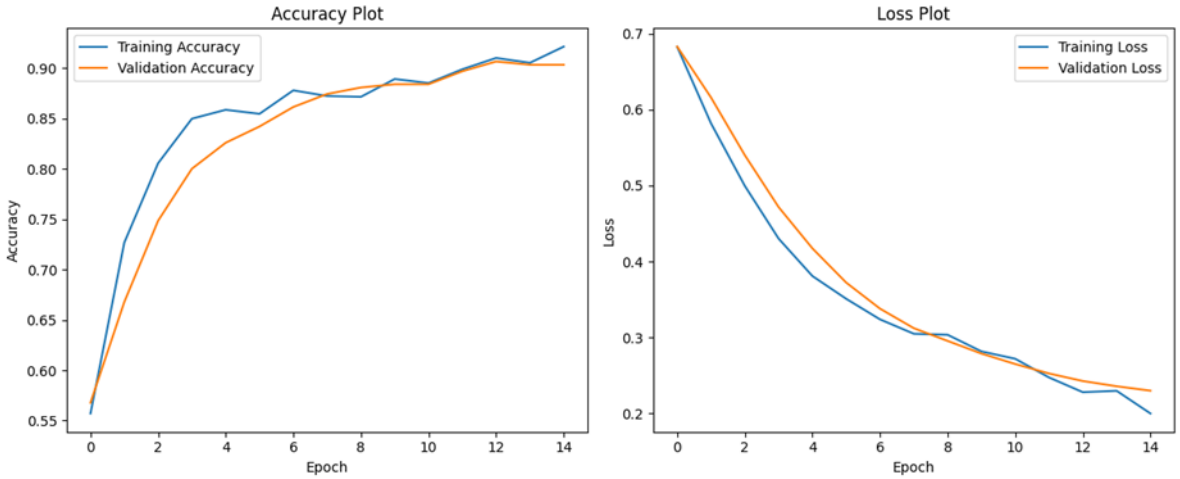

Figure 4.1. The graphics of skin cancer classification on Dullrazor (F1)-filtered images

Figure 4.1 shows the plots of the model trained with images processed by the Dullrazor, or F1 filter. It is clear that the model demonstrates a well-optimized learning process, with steady improvements in both training and validation metrics when looking at the results. Starting with a training accuracy of 55.71% and a validation accuracy of 56.77% in the first epoch, the model consistently improves, reaching 88.91% training accuracy and 88.39% validation accuracy by the tenth epoch. In the final epoch, the model achieves a high training accuracy of 92.12% and validation accuracy of 90.32%, with low training and validation losses, indicating minimal overfitting and strong generalization.

The accuracy and loss plots in Figure 4.1 visually confirm this progress, with the curves rising together and flattening as the model converges. The k-fold cross-validation results, with an average accuracy of 90.32%, further validate the model's robustness and reliability across different data splits, suggesting it should perform well on new data. Overall, these results demonstrate that the model trained with F1-filtered images achieves a high level of performance, balancing learning and generalization effectively, making it suitable for practical applications.

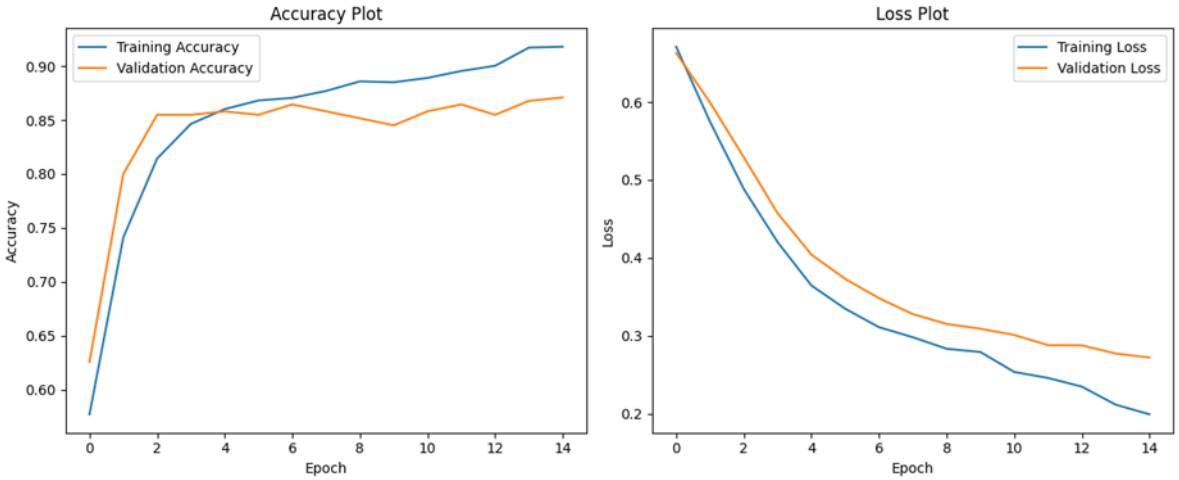

Figure 4.2. The graphics of skin cancer classification on F2-filtered images

Figure 4.2 shows the results of the model trained with images processed by the F2 filter. When examining the results, the model demonstrates a steady learning progression. Starting with a training accuracy of 57.72% and a validation accuracy of 62.58% in the first epoch, the model improves consistently, reaching 86.02% training accuracy and 85.81% validation accuracy by epoch 6, indicating effective learning and generalization.

Around the tenth epoch, the model achieves stable performance with 88.50% training accuracy and 84.52% validation accuracy, showing signs of convergence without overfitting. In the final epoch, the model achieves 91.80% training accuracy and 87.10% validation accuracy, with low loss values, suggesting it has learned effectively from the data.

The accuracy and loss plots confirm this stable learning process, as both curves rise consistently before flattening. The k-fold cross-validation average accuracy of 87.09% further validates the model's robustness, demonstrating that the F2 filter allows the model to generalize well across different data subsets and perform reliably in real-world applications.

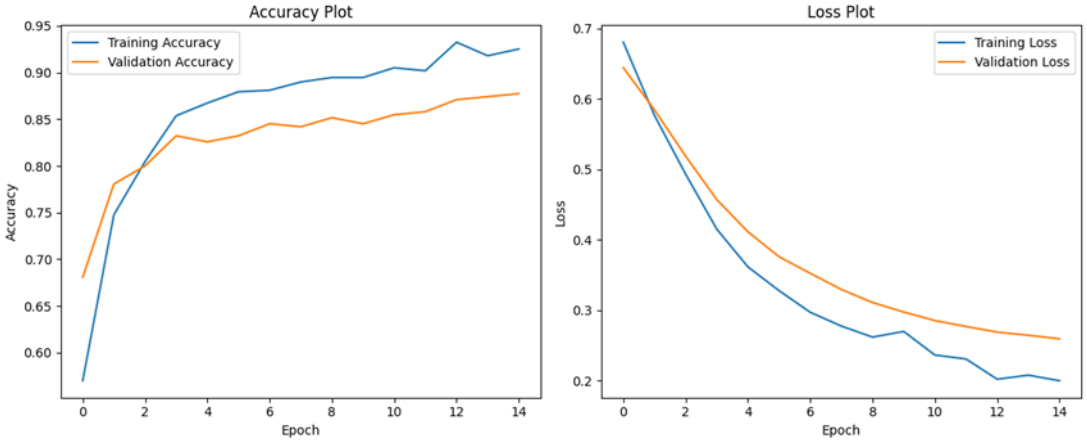

Figure 4.3. The graphics of skin cancer classification on F3-filtered images

When examining the results in Figure 4.3, it's evident that the model follows a strong and stable learning trajectory. In the first epoch, the model starts with a training accuracy of 56.99% and a validation accuracy of 68.06%, establishing a baseline with room for improvement.

As training progresses, the model rapidly improves, reaching 80.47% training accuracy and 80.06% validation accuracy by the third epoch. By epoch 5, training accuracy is at 86.74%, and validation accuracy stabilizes around 82.35%, indicating effective generalization. Around epoch 10, the model achieves balanced performance with a training accuracy of 89.47% and a validation accuracy of 84.52%, showing minimal overfitting and a consistent learning process.

In the final epoch, the model reaches a training accuracy of 92.52% and a validation accuracy of 87.74%, with low loss values, confirming effective learning from the data. The accuracy and loss plots visually support this, as both curves rise steadily and flatten towards the end, signaling convergence.

The k-fold cross-validation results, with an average accuracy of 87.74%, further validate the model's robustness and generalization ability, demonstrating consistent performance across data subsets. Overall, these results indicate that the model trained with the F3 filter has achieved a high level of performance, making it suitable for real-world applications with strong predictive capabilities.

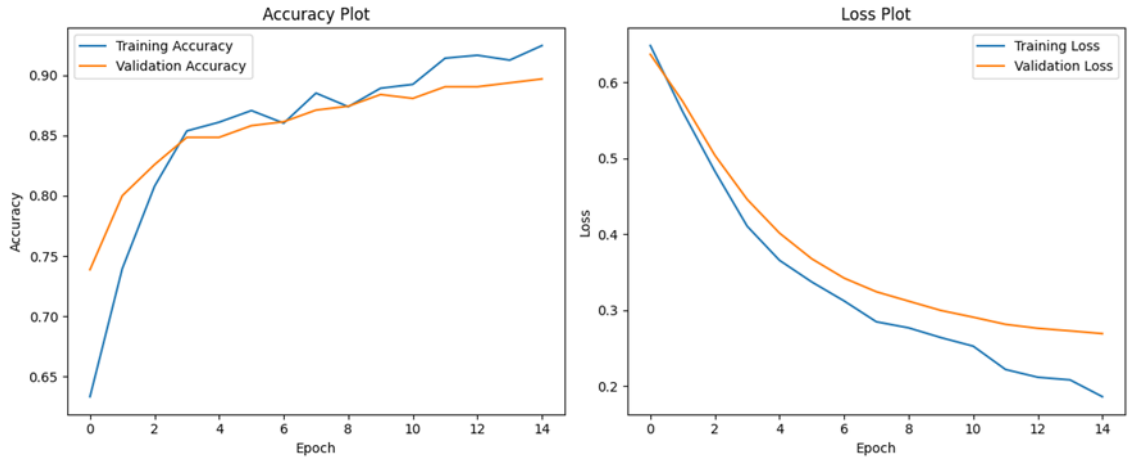

Figure 4.4. The graphics of skin cancer classification on F4 filtered images

According to the plots of Figure 4.4, the training data shows that the model was successfully trained, with consistent improvements in training loss and accuracy from the initial epochs. In the first epoch, the training loss is 0.6486, and the accuracy is 63.34%, while the validation loss is 0.6370, and the validation accuracy is 73.87%. As training progresses, both training and validation accuracy steadily increase, and by the tenth epoch, the validation accuracy is close to 90%, with a significant drop in validation loss.

In the final epoch, the training loss further decreases to 0.1858, with a training accuracy of 92.44%, while the validation accuracy reaches 89.68%. These results indicate strong overall model performance. The consistent rise in accuracy and decrease in losses across epochs suggest an efficient learning process without signs of overfitting.

The accuracy and loss graphs confirm this stability, as training and validation accuracy remain close, and both losses continue to decrease and stabilize. The average accuracy from k-fold validation is 89.67%, reinforcing that the model trained with the F4 filter has achieved reliable performance, making it suitable for practical applications.

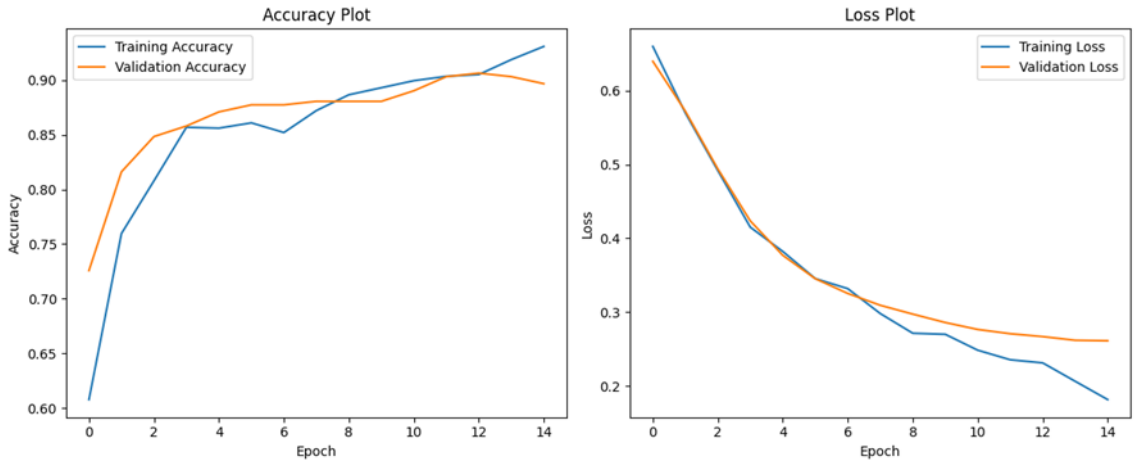

Figure 4.5. The graphics of skin cancer classification on F4-filtered images

The training data is demonstrated in Figure 4.5. shows a continuous and successful learning process, starting with a training accuracy of 60.77% and a validation accuracy of 72.58%, indicating strong generalization from the outset. As training progresses, both accuracy and loss gradually increase. By the third epoch, training accuracy has increased to 80.79%, with validation accuracy at 84.84%, and this rising trend continues throughout.

By the tenth epoch, the model stabilizes with a training accuracy of 88.67% and validation accuracy of 88.06%, indicating that it's effectively differentiating between classes. In the final epoch, the training accuracy reaches 93.09%, and validation accuracy reaches 89.68%, with low losses. This alignment between training and validation metrics suggests strong generalization without overfitting.

The accuracy and loss graphs confirm this trend, with both metrics converging smoothly. The k-fold cross-validation average accuracy of 89.67% further reinforces the model's robustness across data subsets. Overall, the model trained with the F5 filter has achieved a balanced and reliable performance, making it suitable for real-world applications.

When we examine the impact of the F1, F2, F3, F4, and F5 filters on skin cancer classification, we find that each filter contributes differently to the model. Overall, based on the final epoch's training and validation accuracy, loss values, and k-fold validation results, the performance of the filters becomes clear.

The highest performance was achieved with the F1 filter. F1 outperformed other filters in terms of validation accuracy and validation loss, providing strong generalization capabilities with a validation accuracy of 90.32% and low validation loss. Additionally, with an average accuracy of 90.32% in k-fold validation, F1 demonstrated consistent success across different data splits, indicating it as the most effective preprocessing method for skin cancer diagnosis.

The F5 and F4 filters performed well in terms of training accuracy and loss, although they trailed F1 marginally in validation measures. The F5 filter had the best training accuracy (93.09%) and the lowest training loss, indicating good learning on the training set. F4 also produced impressive results, with 92.44% training accuracy and negligible training loss. Both filters achieved validation accuracy of 89.68%, giving them viable alternatives to F1.

The F3 and F2 filters, despite having poorer performance than the other filters, nonetheless gave acceptable accuracy and loss levels. The F3 filter scored a validation accuracy of 87.74%, whereas F2 achieved 87.09%, suggesting modest success. Despite their decreased accuracy, these filters can help with skin cancer diagnosis.

Finally, when the filters' performances are compared, the F1 filter outperforms the others in terms of validation accuracy, validation loss, and k-fold validation average. The F4 and F5 filters demonstrated competitive performance, with excellent training accuracy and low losses, making them viable alternatives to the F1. As a result, F1 looks to be the best filter for diagnosing skin cancer, with F4 and F5 also emerging as strong options.

5. CONCLUSION

Hair removal in dermoscopic images is essential for effective skin cancer identification because hair artefacts can darken critical lesion details and introduce noise, which could hurt the accuracy of diagnosis. As hair differs in type, thickness, and color, the removal requires attentive filtering, which is, in CADs, a part of the preprocessing data. This study mainly focuses on developing various problem-specific filters, and three novel filters were developed for this purpose. Their efficiency is tested by comparison with the two most frequently used filters, Dullrazor and Blackhat, nominated as F1 and F2. Hence, all images of the HAM10000 dataset are processed by five different hair removal filters, from F1 to F5, to measure their impact on skin cancer classification using the Xception model.

The five filters used in the study performed well in hair removal on specific images. The F1 filter performs well on images with sparse hair density, particularly on light-toned skin and light-brown lesions. However, its effectiveness decreases in images with denser and thicker hair. The F2 filter provides balanced results for medium-density hair and pigmented lesions, but it also reduces the details of the lesions in the image. The F3 filter works well on images with light or brown lesions and low hair density. The F4 filter is effective on dark-colored lesions, enhancing contrast and providing effective hair removal. However, its performance is less satisfactory when there is low contrast between the skin and the lesion. Finally, the F5 filter is effective on images with fine hair and pinkish-red lesions, while also successfully removing hair in areas with sparse hair structure.

The findings indicate that each filter has unique strengths, addressing various challenges posed by hair density, lesion shape, and contrast with the skin background. The F1 filter (Dullrazor) demonstrated the highest overall effectiveness, achieving a validation accuracy of 90.32% and showing strong generalization capabilities. Filters F4 and F5 closely followed with validation accuracies of 89.68%, suggesting they could be viable alternatives to F1. The F2 and F3 filters, with validation accuracies of 87.10% and 87.74%, respectively, also contributed positively, although they performed slightly lower than the other filters. Overall, each filter offers distinct advantages, with F1, F4, and F5 emerging as the most effective options for practical applications in skin lesion analysis.

This study provides a solid foundation for our future skin cancer diagnosis research. Moving forward, we aim to develop more effective hair removal methods by combining different AI models with the filters used in this study. By doing so, we seek to offer optimized solutions for various hair types and skin tones, ultimately achieving higher accuracy in diagnostic processes.

REFERENCES

[1] World Health Organization. “Cancer.” World Health Organization. Available: https://www.who.int/health-topics/cancer#tab=tab_1. Accessed: Sep. 15, 2023.

[2] National Cancer Institute. “What Is Cancer?” National Cancer Institute (NIH). Available: https://www.cancer.gov/about-cancer/understanding/what-is-cancer. Accessed: Sep. 15, 2023.

[3] A. Patel, “Benign vs Malignant Tumors,” JAMA Oncology, vol. 6, no. 9, p. 1488, Sep. 2020.

[4] X. Guan, "Cancer metastases: challenges and opportunities," Acta Pharmaceutica Sinica B, vol. 5, pp. 402-418, 2015, doi: 10.1016/j.apsb.2015.07.005.

[5] H. Sung, J. Ferlay, R. Siegel, M. Laversanne, I. Soerjomataram, A. Jemal, and F. Bray, "Global cancer statistics 2020: GLOBOCAN estimates of incidence and mortality worldwide for 36 cancers in 185 countries," CA: A Cancer Journal for Clinicians, vol. 71, pp. 209-249, 2021, doi: 10.3322/caac.21660.

[6] World Health Organization, International Agency for Research on Cancer. "Global Cancer Observatory: Cancer Today." Table: Population and Cancer Types, 2020. Available: https://gco.iarc.who.int/today/en/dataviz/tables?mode=population&types=1&sort_by=value1&group_populations=0&include_nmsc_other=0&cancers=40. Accessed: Nov. 1, 2024.

[7] K. Urban, S. Mehrmal, P. Uppal, R. L. Giesey, and G. R. Delost, “The global burden of skin cancer: A longitudinal analysis from the Global Burden of Disease Study, 1990–2017,” JAAD International, vol. 2, pp. 98–108, Mar. 2021.

[8] C. Fitzmaurice et al., “Global, Regional, and National Cancer Incidence, Mortality, Years of Life Lost, Years Lived with Disability, and Disability-Adjusted Life-years for 32 Cancer Groups, 1990 to 2015,” JAMA Oncology, vol. 3, no. 4, pp. 524-548, Apr. 2017.

[9] World Cancer Research Fund International. “Skin cancer statistics.” World Cancer Research Fund International. Available: https://www.wcrf.org/cancer-trends/skin-cancer-statistics/. Accessed: Sep. 15, 2023.

[10] World Health Organization. “Radiation: Ultraviolet (UV) radiation and skin cancer.” World Health Organization. Available: https://www.who.int/news-room/questions-and-answers/item/radiationultraviolet-(uv)-radiation-and-skin-cancer. Accessed: Sep. 17, 2023.

[11] G. P. Guy, C. C. Thomas, T. Thompson, M. Watson, G. M. Massetti, and L. C. Richardson, “Vital signs: melanoma incidence and mortality trends and projections—United States, 1982–2030,” Morbidity and Mortality Weekly Report (MMWR), vol. 64, no. 21, pp. 591–596, Jun. 2015.

[12] O. Jones, C. Ranmuthu, P. Hall, G. Funston, and F. Walter, "Recognising Skin Cancer in Primary Care," Advances in Therapy, vol. 37, pp. 603-616, 2019, doi: 10.1007/s12325-019-01130-1.

[13] J. Frühauf et al., “Patient acceptance and diagnostic utility of automated digital image analysis of pigmented skin lesions,” Journal of the European Academy of Dermatology and Venereology, vol. 26, no. 3, pp. 368–372, Apr. 2011.

[14] Y. Li and L. Shen, “Skin Lesion Analysis towards Melanoma Detection Using Deep Learning Network,” Sensors (Basel, Switzerland), vol. 18, 2017, doi: 10.3390/s18020556.

[15] Y. Xie, J. Zhang, Y. Xia, and C. Shen, “A Mutual Bootstrapping Model for Automated Skin Lesion Segmentation and Classification,” IEEE Transactions on Medical Imaging, vol. 39, pp. 2482-2493, 2019, doi: 10.1109/TMI.2020.2972964.

[16] J. Marks and J. Miller, “Structure and Function of the Skin,” in Lookingbill and Marks' Principles of Dermatology, 2019, doi: 10.1016/B978-1-4557-2875-6.00002-9.

[17] ACCESS Virtual Learning, “2.02 Skin Layers and Functions,” [Online]. Available: https://accessdl.state.al.us/AventaCourses/access_courses/anatomy_ua_v17/02_unit/02-02/02-02_text2.html. Accessed: May 17, 2024.

[18] V. C. Scanlon and T. Sanders, Essentials of anatomy and physiology. F. A. Davis, 2018.

[19] A. Waugh and A. Grant, Anatomy and physiology in health and illness, 2009.

[20] D. B. Light and D. A. Cooley, Cells, tissues, and skin. Infobase Publishing, 2009.

[21] Cleveland Clinic, “Hypodermis (Subcutaneous Tissue): Function & Structure,” [Online]. Available: https://my.clevelandclinic.org/health/body/21902-hypodermis-subcutaneous-tissue. Accessed: May 17, 2024.

[22] K. Tanese, "Diagnosis and Management of Basal Cell Carcinoma," Current Treatment Options in Oncology, vol. 20, pp. 1-13, 2019, doi: 10.1007/s11864-019-0610-0.

[23] A. Hawrot, M. Alam, and D. Ratner, "Squamous cell carcinoma," Current Problems in Dermatology, vol. 15, pp. 91-133, 2003, doi: 10.1016/S1040-0486(03)00005-X.

[24] N. Treiber, M. A. Huber, K. Scharffetter-Kochanek, and L. Schneider, "Early detection of skin cancer," MMW Fortschritte der Medizin, vol. 156, no. 4, pp. 37–40, 2014.

[25] L. Fania, D. Didona, R. Morese, I. Campana, V. Coco, F. D. Di Pietro, F. Ricci, S. Pallotta, E. Candi, D. Abeni, and E. Dellambra, "Basal Cell Carcinoma: From Pathophysiology to Novel Therapeutic Approaches," Biomedicines, vol. 8, 2020.

[26] C. Margo and K. Waltz, "Basal cell carcinoma of the eyelid and periocular skin," Survey of Ophthalmology, vol. 38, no. 2, pp. 169-192, 1993.

[27] R. Bariani, F. Nahas, M. V. Barbosa, A. B. Farah, and L. Ferreira, "Basal cell carcinoma: an updated epidemiological and therapeutically profile of an urban population," Acta Cirurgica Brasileira, vol. 21, no. 2, pp. 66-73, 2006.

[28] DermNet NZ, “Superficial basal cell carcinoma images,” [Online]. Available: https://dermnetnz.org/images/superficial-basal-cell-carcinoma-images. Accessed: May 17, 2024.

[29] American Cancer Society, “Skin cancer image gallery,” [Online]. Available: https://www.cancer.org/cancer/types/skin-cancer/skin-cancer-image-gallery.html. Accessed: May 17, 2024.

[30] K. Peris et al., "Diagnosis and treatment of basal cell carcinoma: European consensus-based interdisciplinary guidelines," European Journal of Cancer, vol. 118, pp. 10-34, 2019.

[31] K. Mosterd et al., "Surgical excision versus Mohs' micrographic surgery for primary and recurrent basal-cell carcinoma of the face: a prospective randomised controlled trial with 5-years' follow-up," The Lancet Oncology, vol. 9, no. 12, pp. 1149-1156, 2008.

[32] C. Berking, A. Hauschild, O. Kölbl, G. Mast, and R. Gutzmer, "Basal cell carcinoma-treatments for the commonest skin cancer," Deutsches Arzteblatt International, vol. 111, no. 22, pp. 389-395, 2014.

[33] S. Bali, E. Deif, and A. Rajeev, "Treatment of basal cell carcinoma: An overview," Journal of Skin and Sexually Transmitted Diseases, 2022.

[34] J. Verkouteren, K. Ramdas, M. Wakkee, and T. Nijsten, "Epidemiology of basal cell carcinoma: scholarly review," British Journal of Dermatology, vol. 177, 2017.

[35] G. D. Goldman, "Squamous cell cancer: A practical approach," Semin. Cutan. Med. Surg., vol. 17, p. 80, 1998.

[36] R. E. Kwa, K. Campana, and R. L. Moy, "Biology of cutaneous squamous cell carcinoma," J. Am. Acad. Dermatol., vol. 26, p. 1, 1992.

[37] T. M. Johnson, D. E. Rowe, B. R. Nelson, and N. A. Swanson, "Squamous cell carcinoma of the skin (excluding lip and oral mucosa)," J. Am. Acad. Dermatol., vol. 26, p. 467, 1992.

[38] R. S. Stern, "PUVA Follow-Up Study. The risk of squamous cell and basal cell cancer associated with psoralen and ultraviolet A therapy: a 30-year prospective study," J. Am. Acad. Dermatol., vol. 66, pp. 553–562, 2012.

[39] R. Marks, "Squamous cell carcinoma," Lancet, vol. 347, p. 735, 1996.

[40] American Cancer Society, Cancer Facts & Figures 2011. Atlanta: American Cancer Society, 2011. [Online]. Available: https://www.cancer.org/content/dam/cancer-org/research/cancer-facts-and-statistics/annual-cancer-facts-and-figures/2011/cancer-facts-and-figures-2011.pdf

[41] R. L. Moy, "Clinical presentation of actinic keratoses and squamous cell carcinoma," J. Am. Acad. Dermatol., vol. 42, no. 1, pp. S8-S10, 2000.

[42] D. D. Yang et al., “Trends in keratinocyte skin cancer incidence, mortality and burden of disease in 33 countries between 1990 and 2017,” Br. J. Dermatol., vol. 188, no. 2, pp. 237-246, 2022.

[43] M. Wehner et al., “All-cause mortality in patients with basal and squamous cell carcinoma: A systematic review and meta-analysis,” J. Am. Acad. Dermatol., vol. 78, no. 4, pp. 663–672, 2017.

[44] A. Ø. Jensen, A. Lamberg, J. Jacobsen, A. B. Olesen, and H. Sørensen, “Nonmelanoma skin cancer and ten-year all-cause mortality: a population-based cohort study,” Acta Derm. Venereol., vol. 90, no. 4, pp. 362–367, 2010.

[45] H. Kanavy and M. Gerstenblith, “Ultraviolet radiation and melanoma,” Seminars in Cutaneous Medicine and Surgery, vol. 30, no. 4, pp. 222-228, 2011.

[46] M. Rastrelli, S. Tropea, C. Rossi, and M. Alaibac, “Melanoma: epidemiology, risk factors, pathogenesis, diagnosis and classification,” In Vivo, vol. 28, no. 6, pp. 1005-1011, 2014.

[47] R. Friedman, D. Rigel, and A. Kopf, “Early detection of malignant melanoma: The role of physician examination and self-examination of the skin,” CA: A Cancer Journal for Clinicians, vol. 35, no. 3, pp. 130-151, 1985.

[48] D. Shenenberger, “Cutaneous malignant melanoma: a primary care perspective,” American Family Physician, vol. 85, no. 2, pp. 161-168, 2012.

[49] F. Bray, J. Ferlay, I. Soerjomataram, R. Siegel, L. A. Torre, and A. Jemal, “Global cancer statistics 2018: GLOBOCAN estimates of incidence and mortality worldwide for 36 cancers in 185 countries,” CA: A Cancer Journal for Clinicians, vol. 68, pp. 394-424, 2018.

[50] J. Melia et al., “The relation between mortality from malignant melanoma and early detection in the Cancer Research Campaign Mole Watcher Study,” British Journal of Cancer, vol. 85, pp. 803-807, 2001.

[51] J. Schneider, D. Moore, and M. Mendelsohn, “Screening program reduced melanoma mortality at the Lawrence Livermore National Laboratory, 1984 to 1996,” Journal of the American Academy of Dermatology, vol. 58, no. 5, pp. 741-749, 2006.

[52] M. Arnold et al., “Global burden of cutaneous melanoma in 2020 and projections to 2040,” JAMA Dermatology, vol. 158, 2022.

[53] R. Spanjaard, D. T. Weaver, S. Erramilli, and P. Mohanty, “Perspective: Melanoma diagnosis and monitoring: Sunrise for melanoma therapy but early detection remains in the shade,” arXiv: Tissues and Organs, 2015.

[54] S. Jang, T. Poretta, T. Bhagnani, Q. Harshaw, M. Burke, and S. Rao, “Real-World Recurrence Rates and Economic Burden in Patients with Resected Early-Stage Melanoma,” Dermatology and Therapy, vol. 10, pp. 985–999, 2020.

[55] A. Eftekhari, E. Ahmadian, S. Salatin, S. Sharifi, S. M. Dizaj, and M. Hasanzadeh, “Current analytical approaches in diagnosis of melanoma,” TrAC Trends in Analytical Chemistry, 2019.

[56] D. Rigel, J. E. Russak, and R. Friedman, “The Evolution of Melanoma Diagnosis: 25 Years Beyond the ABCDs,” CA: A Cancer Journal for Clinicians, vol. 60, 2010.

[57] Canadian Skin Cancer Foundation, "Skin Check: How to Perform Self-Examination," Early Detection, [online]. Available: https://www.canadianskincancerfoundation.com/early-detection/skin-check/. Accessed: Nov. 1, 2024.

[58] N. R. Abbasi, H. Shaw, D. Rigel, R. Friedman, W. McCarthy, I. Osman, A. Kopf, and D. Polsky, “Early diagnosis of cutaneous melanoma: revisiting the ABCD criteria,” JAMA, vol. 292, no. 22, pp. 2771-2776, 2004.

[59] Wikipedia, "Dermatoscopy," Wikipedia, The Free Encyclopedia, [online]. Available: https://en.wikipedia.org/wiki/Dermatoscopy. Accessed: Nov. 1, 2024.

[60] G. Ferrara et al., “Dermoscopy of pigmented skin lesions--a valuable tool for early diagnosis of melanoma,” The Lancet Oncology, vol. 2, no. 7, pp. 443-449, 2001.

[61] M. Bafounta, A. Beauchet, P. Aegerter, and P. Saiag, “Is dermoscopy (epiluminescence microscopy) useful for the diagnosis of melanoma? Results of a meta-analysis using techniques adapted to the evaluation of diagnostic tests,” Archives of Dermatology, vol. 137, no. 10, pp. 1343–1350, 2001.

[62] M. Vestergaard, P. Macaskill, P. E. Holt, and S. Menzies, “Dermoscopy compared with naked eye examination for the diagnosis of primary melanoma: a meta-analysis of studies performed in a clinical setting,” British Journal of Dermatology, vol. 159, 2008.

[63] H. Kittler, H. Pehamberger, K. Wolff, and M. Binder, “Diagnostic accuracy of dermoscopy,” The Lancet Oncology, vol. 3, no. 3, pp. 159-165, 2002.

[64] J. Premaladha and K. S. Ravichandran, “Novel Approaches for Diagnosing Melanoma Skin Lesions Through Supervised and Deep Learning Algorithms,” Journal of Medical Systems, vol. 40, no. 1, pp. 1–12, 2016.

[65] M. Marchetti et al., “Results of the 2016 International Skin Imaging Collaboration International Symposium on Biomedical Imaging Challenge: Comparison of the Accuracy of Computer Algorithms to Dermatologists for the Diagnosis of Melanoma from Dermoscopic Images,” Journal of the American Academy of Dermatology, vol. 78, no. 2, pp. 270–277.e1, 2018.

[66] S. Mittal and Y. Hasija, “Applications of Deep Learning in Healthcare and Biomedicine,” in Applications of Artificial Intelligence in Cancer Diagnosis and Therapy, 2019, pp. 57–77.

[67] C. Tong, L. Medsker, L. Cheng, A. Jafari, and X. Wang, “Introduction to the special issue on deep learning for biomedical and healthcare applications,” Neural Computing and Applications, vol. 30, no. 8, pp. 2015–2016, 2018.

[68] A. Sedik et al., “Deploying machine and deep learning models for efficient data-augmented detection of COVID-19 infections,” Viruses, vol. 12, 2020.

[69] S. Silvestrini and M. Lavagna, “Deep Learning and Artificial Neural Networks for Spacecraft Dynamics, Navigation and Control,” Drones, vol. 6, no. 10, 2022.

[70] Y. LeCun, Y. Bengio, and G. Hinton, "Deep learning," Nature, vol. 521, no. 7553, pp. 436–444, 2015.

[71] I. Goodfellow, Y. Bengio, and A. Courville, Deep Learning, Cambridge, MA: MIT Press, 2016.

[72] "Introduction to Neural Networks," Electronics World, accessed Nov. 1, 2024. [Online]. Available: https://www.electronicsworld.co.uk/introduction-to-neural-networks/12544/

[73] D. A. Purves et al., Neuroscience, 5th ed., Sunderland, MA: Sinauer Associates, 2012.

[74] S. Haykin, Neural Networks and Learning Machines, 3rd ed., New York, NY, USA: Pearson, 2009.

[75] J. Schmidhuber, "Deep learning in neural networks: An overview," Neural Networks, vol. 61, pp. 85–117, Jan. 2015.

[76] A. Krizhevsky, I. Sutskever, and G. E. Hinton, "ImageNet classification with deep convolutional neural networks," in Proc. Advances in Neural Information Processing Systems (NIPS), vol. 25, 2012, pp. 1097–1105.

[77] D. E. Rumelhart, G. E. Hinton, and R. J. Williams, "Learning representations by back-propagating errors," Nature, vol. 323, no. 6088, pp. 533–536, 1986.

[78] M. Nielsen, Neural Networks and Deep Learning, Determination Press, 2015.

[79] Y. LeCun, L. Bottou, Y. Bengio, and P. Haffner, "Gradient-based learning applied to document recognition," Proceedings of the IEEE, vol. 86, no. 11, pp. 2278–2324, 1998.

[80] K. Simonyan and A. Zisserman, "Very deep convolutional networks for large-scale image recognition," arXiv preprint arXiv:1409.1556, 2014.

[81] K. He, X. Zhang, S. Ren, and J. Sun, "Deep residual learning for image recognition," in Proc. IEEE Conf. Computer Vision and Pattern Recognition (CVPR), 2016, pp. 770–778

[82] G. Huang, Z. Liu, L. Van Der Maaten, and K. Q. Weinberger, "Densely connected convolutional networks," in Proc. IEEE Conf. Computer Vision and Pattern Recognition (CVPR), 2017, pp. 4700–4708.

[83]"The Architecture of LeNet-5," Analytics Vidhya, Mar. 23, 2021. [Online]. Available: https://www.analyticsvidhya.com/blog/2021/03/the-architecture-of-lenet-5/. Accessed: Nov. 1, 2024.

[84] S. B. Bhate, "AlexNet Architecture Explained," Medium, [online]. Available: https://medium.com/@siddheshb008/alexnet-architecture-explained-b6240c528bd5. Accessed: Nov. 1, 2024.

[85]"VGG," Papers with Code, [online]. Available: https://paperswithcode.com/method/vgg. Accessed: Nov. 1, 2024.

[86] C. Szegedy et al., "Going deeper with convolutions," in Proc. IEEE Conf. Computer Vision and Pattern Recognition (CVPR), 2015, pp. 1–9.

[87] M. Yang, L. Cheng, M. Cao, and X. Yan, "A Stacking Ensemble Learning Method to Classify the Patterns of Complex Road Junctions," ISPRS International Journal of Geo-Information, vol. 11, no. 10, p. 523, 2022. doi: 10.3390/ijgi11100523.

[88]"Residual neural network," Wikipedia, The Free Encyclopedia, [online]. Available: https://en.wikipedia.org/wiki/Residual_neural_network. Accessed: Nov. 1, 2024.

[89]"ResNet," Dive into Deep Learning, [online]. Available: https://d2l.ai/chapter_convolutional-modern/resnet.html#fig-resnet18. Accessed: Nov. 1, 2024.

[90] A. S. Sohail, M. M. Habib, and M. A. Wahab, "A Deep Learning Method for Early Detection of Diabetic Foot Using Decision Fusion and Thermal Images," Applied Sciences, vol. 12, no. 15, p. 7524, 2022. doi: 10.3390/app12157524.

[91] F. Chollet, "Xception: Deep learning with depthwise separable convolutions," in Proc. IEEE Conf. Computer Vision and Pattern Recognition, 2017.

[92] F. Sultonov et al., "Mixer U-Net: An Improved Automatic Road Extraction from UAV Imagery," Applied Sciences, vol. 12, p. 1953, 2022.

[93] C. Szegedy et al., “Rethinking the Inception Architecture for Computer Vision,” arXiv:1512.00567, Dec. 2015. [Online]. Available: https://arxiv.org/abs/1512.00567v3

[94] P. Tschandl, C. Rosendahl, and H. Kittler, "The HAM10000 dataset, a large collection of multi-source dermatoscopic images of common pigmented skin lesions," Scientific Data, vol. 5, article no. 180161, 2018.

[95] ISIC Archive, "The International Skin Imaging Collaboration (ISIC): Melanoma Project," [Online]. Available: https://www.isic-archive.com. Accessed: Nov. 1, 2024.

[96] R. Mendonça et al., "PH²- A dermoscopic image database for research and benchmarking," in Proc. IEEE Engineering in Medicine and Biology Society (EMBC), 2013, pp. 5437–5440.

[97] S. Pacheco et al., "Derm7pt: A clinical skin cancer dataset for training machine learning algorithms," in Proc. IEEE International Symposium on Biomedical Imaging (ISBI), 2020, pp. 1684–1688.

[98] M. Combalia et al., "BCN20000: Dermoscopic lesions in the wild," arXiv preprint arXiv:1908.02288, 2019.

[99] S. Osman, H. Maher, and B. Sayed, "Skin Cancer Detection Using Deep Learning," Journal of the ACS Advances in Computer Science, 2023.

[100] R. A. Mehr and A. Ameri, "Skin Cancer Detection Based on Deep Learning," Journal of Biomedical Physics & Engineering, vol. 12, pp. 559–568, 2022.

[101] A. Imran, A. Nasir, M. Bilal, G. Sun, A. Alzahrani, and A. Almuhaimeed, "Skin Cancer Detection Using Combined Decision of Deep Learners," IEEE Access, vol. 10, pp. 118198–118212, 2022.

[102] H. Singh, S. Kaushik, S. Talyan, and K. Dwivedi, "Skin Cancer Detection Using Deep Learning Techniques," International Journal for Research in Applied Science and Engineering Technology, 2022.

[103] A. M. Obaid, A. S. Shawkat, and N. S. Abdulhussein, "A powerful deep learning method for skin cancer detection," Journal of Autonomous Intelligence, vol. 7, no. 1, 2023.

[104] J. Amin, A. Sharif, N. Gul, M. A. Anjum, M. W. Nisar, F. Azam, and S. A. C. Bukhari, "Integrated design of deep features fusion for localization and classification of skin cancer," Pattern Recognition Letters, 2019. doi: 10.1016/j.patrec.2019.11.042.

[105] T. Majtner, B. Bajić, S. Yildirim, J. Y. Hardeberg, J. Lindblad, and N. Sladoje, "Ensemble of convolutional neural networks for dermoscopic images classification," arXiv preprint arXiv:1808.05071, 2018.

[106] K. Thurnhofer-Hemsi and E. Domínguez, "A convolutional neural network framework for accurate skin cancer detection," Neural Processing Letters, vol. 53, no. 5, pp. 3073–3093, 2021.

[107] N. Codella et al., "Skin lesion analysis toward melanoma detection: A challenge at the 2018 International Skin Imaging Collaboration (ISIC)," arXiv preprint arXiv:1902.03368, 2019.

[108] W. Gouda, N. Sama, G. Al-Waakid, M. Humayun, and N. Jhanjhi, "Detection of skin cancer based on skin lesion images using deep learning," Healthcare, vol. 10, no. 7, p. 1183, 2022. doi: 10.3390/healthcare10071183.

[109] N. Nida, A. Irtaza, A. Javed, M. H. Yousaf, and M. T. Mahmood, “Melanoma lesion detection and segmentation using deep region based convolutional neural network and fuzzy C-means clustering,” Int. J. Med. Inform., vol. 124, pp. 37–48, 2019, doi: 10.1016/j.ijmedinf.2019.01.005.

[110] G. Alwakid, W. Gouda, M. Humayun, and N. Sama, "Melanoma Detection Using Deep Learning-Based Classifications," Healthcare, vol. 10, no. 12, p. 2481, Dec. 2022.

[111] T. DeVries and D. Ramachandram, "Skin Lesion Classification Using Deep Multi-Scale Convolutional Neural Networks," arXiv preprint arXiv:1703.01402, 2017.

[112] M. Shorfuzzaman, "An explainable stacked ensemble of deep learning models for improved melanoma skin cancer detection," Multimedia Systems, vol. 28, pp. 1309–1323, 2022. doi: 10.1007/s00530-021-00787-5.

[113] R. Ogundokun et al., "Enhancing Skin Cancer Detection and Classification in Dermoscopic Images through Concatenated MobileNetV2 and Xception Models," Bioengineering, vol. 10, 2023. doi: 10.3390/bioengineering10080979.

[114] J. Rashid et al., "Skin Cancer Disease Detection Using Transfer Learning Technique," Applied Sciences, vol. 12, 2022. doi: 10.3390/app12115714.

[115] A. Mehmood et al., “SBXception: A shallower and broader Xception architecture for efficient classification of skin lesions,” Cancers, vol. 15, no. 14, p. 3604, 2023, doi: 10.3390/cancers15143604.

[116] S. Das and K. Sharma, "Inception-ResNet-V2 Based Skin Lesion Classification for Early Detection and Treatment," in 2023 Int. Conf. Computational Intelligence for Information, Security and Communication Applications (CIISCA), Bengaluru, India, 2023, pp. 143-146, doi: 10.1109/CIISCA59740.2023.00037.

[117] I. Ahmad, J. Amin, M. IkramUllah Lali, F. Abbas, and M. Imran Sharif, “A novel deeplabv3+ and vision-based Transformer model for segmentation and classification of skin lesions,” Biomedical Signal Processing and Control, vol. 92, p. 106084, Jun. 2024. doi: 10.1016/j.bspc.2024.106084.

[118] L. Wei, K. Ding, and H. Hu, "Automatic Skin Cancer Detection in Dermoscopy Images Based on Ensemble Lightweight Deep Learning Network," IEEE Access, vol. 8, pp. 99633-99647, 2020, doi: 10.1109/ACCESS.2020.2997710.

[119] S. S. Lee, “Advanced Skin Cancer Detection using Hybrid CNN Feature Extraction,” International Journal of Scientific Research and Engineering Trends, vol. 10, no. 5, pp. 2261–2265, Oct. 2024, doi: 10.61137/ijsret.vol.10.issue5.287.

[120] D. Chakraborti, R. Kaur, S. Umbaugh, and R. LeAnder, “An effective hair detection algorithm for dermoscopic melanoma images of skin lesions,” Applications of Digital Image Processing XXXIX, vol. 9971, p. 997104, Sep. 2016, doi: 10.1117/12.2236565.

[121] H. Zhou et al., “Feature-preserving artifact removal from dermoscopy images,” Medical Imaging 2008: Image Processing, vol. 6914, p. 69141B, Mar. 2008, doi: 10.1117/12.770824.

[122] D. Chakraborti, R. Kaur, S. Umbaugh, and R. LeAnder, “An effective hair detection algorithm for dermoscopic melanoma images of skin lesions,” Applications of Digital Image Processing XXXIX, vol. 9971, p. 997104, Sep. 2016, doi: 10.1117/12.2236565.

[123] T. Lee, V. Ng, R. Gallagher, A. Coldman, and D. McLean, "Dullrazor®: A software approach to hair removal from images," Computers in Biology and Medicine, vol. 27, no. 6, pp. 533-543, 1997.

[124] F.-Y. Xie, S.-Y. Qin, Z.-G. Jiang, and R.-S. Meng, “PDE-based unsupervised repair of hair-occluded information in dermoscopy images of melanoma,” Computerized Medical Imaging and Graphics, vol. 33, no. 4, pp. 275–282, Jun. 2009, doi: 10.1016/j.compmedimag.2009.01.003.

[125] K. Kiani and A. R. Sharafat, “E-shaver: An improved DullRazor® for digitally removing dark and light-colored hairs in dermoscopic images,” Computers in Biology and Medicine, vol. 41, no. 3, pp. 139–145, Mar. 2011, doi: 10.1016/j.compbiomed.2011.01.003.

[126] A. Huang, S.-Y. Kwan, W.-Y. Chang, M.-Y. Liu, M.-H. Chi, and G.-S. Chen, "A robust hair segmentation and removal approach for clinical images of skin lesions," in Proc. 35th Annu. Int. Conf. IEEE Eng. Med. Biol. Soc. (EMBC), Osaka, Japan, 2013, pp. 3315-3318, doi: 10.1109/EMBC.2013.6610250.

[127] B. Yılmaz and A. Tandiroviç Gürsel, "Cilt kanseri tanısında tıbbi görüntüleri kıldan temizlemek için kullanılan iki yeni filtre," Çukurova Üniversitesi Mühendislik Fakültesi Dergisi, vol. 38, no. 4, pp. 1139-1149, 2023, doi: 10.21605/cukurovaumfd.1410803.

[128] T. Yalçın and A. Tandirovic Gürsel, “Improving Digital Image Quality for Convolution Neural Network Based Computer-Aided Diagnosis (CNN-CAD) of Skin Cancer,” Çukurova Üniversitesi Mühendislik Fakültesi Dergisi, vol. 36, no. 4, pp. 1099-1110, 2021. doi: 10.21605/cukurovaumfd.1048370.

[129] Massachusetts Institute of Technology, "Introduction to Communication, Control, and Signal Processing, Chapter 11," MIT OpenCourseWare, 2010. [Online]. Available: https://ocw.mit.edu/courses/6-011-introduction-to-communication-control-and-signal-processing-spring-2010/f135b328c7448bf21c4939ea9ff8f8fb_MIT6_011S10_chap11.pdf

[130] "Top hat transform," Wikipedia, The Free Encyclopedia. [Online]. Available: https://en.wikipedia.org/wiki/Top-hat_transform. Accessed: Jan. 20, 2024.

[131] K. Zuiderveld, “Contrast Limited Adaptive Histogram Equalization,” in Graphics Gems IV, Academic Press Professional, Inc., USA, pp. 474-485, 1994.

[132] "Thresholding Operations using OpenCV," OpenCV Documentation. [Online]. Available: https://docs.opencv.org/3.4/d7/d4d/tutorial_py_thresholding.html. Accessed: Nov. 1, 2024.

[133] J. C. Church, Y. Chen, and S. V. Rice, "A Spatial Median Filter for Noise Removal in Digital Images," in Proc. IEEE Int. Conf. on Image Processing, 2008, pp. 618-623.

[134] A. Telea, “An Image Inpainting Technique Based on the Fast-Marching Method,” Journal of Graphics Tools, vol. 9, no. 1, pp. 23–34, Jan. 2004, doi: 10.1080/10867651.2004.10487596.

[135] I. Bouganssa, M. Sbihi, and M. Zaim, “Laplacian Edge Detection Algorithm for Road Signal Images and FPGA Implementation,” International Journal of Machine Learning and Computing, vol. 9, no. 1, pp. 57–61, 2019, doi: 10.18178/ijmlc.2019.9.1.765.

[136] R. C. Gonzalez and P. Wintz, Digital Image Processing, 3rd ed., Upper Saddle River, NJ, USA: Prentice Hall, 2002.